CHALMERS
UNIVERSITY OF TECHNOLOGY

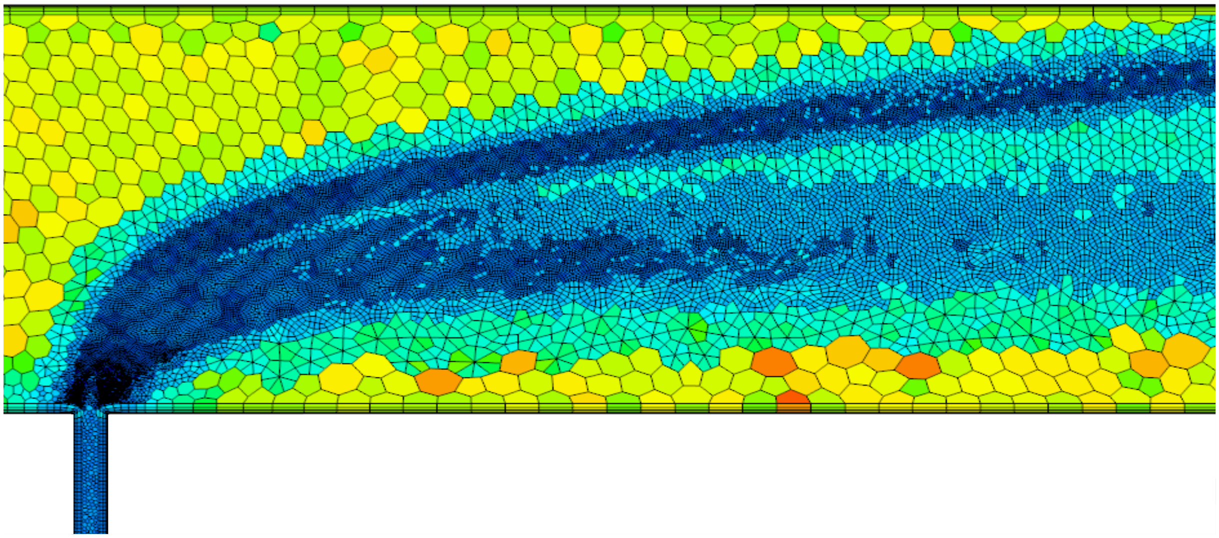

Analysis of Fuel-Air Mixing in Jet in Crossflow

Master's Thesis in Innovative and Sustainable Chemical Engineering

WASINEE CHAROENCHANG

DEPARTMENT OF CHEMISTRY AND CHEMICAL ENGINEERING

CHALMERS UNIVERSITY OF TECHNOLOGY

Gothenburg, Sweden 2021
www.chalmers.se

MASTER’S THESIS 2021

Analysis of Fuel-Air Mixing in Jet in Crossflow

WASINEE CHAROENCHANG

Department of Chemistry and Chemical Engineering
CHALMERS UNIVERSITY OF TECHNOLOGY
Gothenburg, Sweden 2021

Analysis of Fuel-Air Mixing in Jet in Crossflow
WASINEE CHAROENCHANG

Academic supervisor and examiner: Prof. Ronnie Andersson
Industrial supervisor: Dr. Daniel Lörstad

Department of Chemistry and Chemical Engineering
Chalmers University of Technology
SE-412 96 Gothenburg
Sweden
Telephone + 4631 772 1000
www.chalmers.se

In *cooperation* with:
Siemens Energy AB
SE-612 31 Finspång
Sweden
Telephone + 46 122 810 00
www.siemens-energy.com

Cover: A mesh scene obtained from STAR CCM+ when adaptive mesh refinement was applied to jet in crossflow configuration

Gothenburg, Sweden, 2021

Analysis of Fuel-Air Mixing in Jet in Crossflow
WASINEE CHAROENCHANG
Department of Chemistry and Chemical Engineering
Chalmers University of Technology

Abstract

With the growth of energy demand nowadays, environmental concern of NO_x emission from gas turbines has been increasing in attention. NOx emission can be lowered by decreasing the local maximum temperature which results from a good premixing of air and fuel. The mixing performance is affected by location of the fuel holes on the fuel pins which can be optimized using computational fluid dynamics. However, the computational mesh is known to be an important parameter which affect solution convergence and accuracy, thus it is significant to be optimized. The main goal was to develop the new mesh strategy and confirm grid independence to achieve higher accuracy with minimum number of cells.

This thesis study applied a typical jet in crossflow (JIC) configuration to analyze the mixing of fuel and air in gas turbines related to fuel injection nozzles and Siemens PLM's STAR-CCM+ was chosen as a software. Previously used mesh strategies in SGT-750, SGT-800 and other projects in Siemens Energy AB were investigated in terms of grid independence properties and accuracy compared to the experimental data presented by F. Galeazzo et al. [1]. The results revealed that the mesh required improvement.

Model dependence test including realizable k-epsilon, LES, lag EB k-epsilon and SST k-omega was performed. The choice of turbulence model was found to be important to achieve reliable predictions of the flow. Realizable k-epsilon and LES were the most suitable models for JIC simulation. To achieve good flow resolution, evaluated by turbulent kinetic energy and subgrid viscosity ratio, the cell sizes were properly identified by Kolmogorov and Taylor microscales. A successful mesh optimization approach was achieved by combining the best previously used mesh strategy and adaptive mesh refinement with respect to the concentration gradient. The optimized mesh exhibited high grid independency and the velocity and concentration fields agreed well with available experimental data. Therefore, the static optimized mesh is recommended to be used for future optimization of the fuel hole distribution in gas turbines.

Key words: Computational Fluid Dynamic, Jet in Crossflow, Grid Independency, Adaptive Mesh Refinement, Mesh Optimization, Gas Turbine Burner

Acknowledgement

This thesis was performed in cooperation with the research and development combustion team at Siemens Energy AB, Sweden during January to June 2021 through COVID pandemic period. I would like to thank my industrial supervisor at Siemens Energy AB, Dr. Daniel Lörstad for his kind guidance and support throughout the thesis. I would also like to thank other colleagues at Siemens Energy AB that have provided support and suggestions together with feedback on my thesis. In addition, I would like to express my gratitude to Saeid Kharazmi, my manager at Siemens Energy AB for granting me opportunity to perform the thesis and for guidance since my first day at the company. Special thanks to my academic supervisor and examiner, Prof. Ronnie Andersson at Chalmers University of Technology for supporting and providing an academic perspective of the thesis work. Last but not least, many thanks to my family and friends who have supported me kindly.

Göteborg, 2021-10-12

Wasinee Charoenchang

Nomenclature

Acronyms

Abbreviation	Meaning
AMR	Adaptive Mesh Refinement
CAE	Computational Aided Engineer
CFD	Computational Fluid Dynamics
CFL	Courant Friedrichs Lewy
CO	Carbon Monoxide
CO_2	Carbon Dioxide
DLE	Dry Low Emission
JIC	Jet in Crossflow
Lag EB	Lag Elliptic Blending
LES	Large Eddy Simulation
LIF	Laser Induced Fluorescence
NOx	Nitrogen Oxide
PIV	Particle Image Velocimetry
RANS	Reynolds Averaged Navier-Stokes
RMS	Root Mean Square
RPL	Rich Pilot Lean
RST	Reynolds Stress Transport
SST	Shear Stress Transport
STAL	Svenska Turbinfabriks Aktiebolaget Ljungström
STAR-CCM+	Commercial CFD software
WALE	Wall-Adapting Local-Eddy Viscosity
WLE	Wet Low Emission

Greek letters

Symbol	Meaning	Unit
α	Elliptic blending factor	-
β	Coefficient of thermal expansion	1/K
ε	Turbulence dissipation rate	m^2/s^3
λ	Taylor microscale	m
μ	Dynamic viscosity	kg/ms
μ_t	Turbulent viscosity	kg/ms
ν	Instantaneous velocity	m/s
ν_c	Velocity of sound	m/s
υ	Kinematic viscosity	m^2/s
ρ	Density	kg/m^3
σ	Stress tensor	N/m^2
τ	Shear stress tensor	N/m^2
τ_{RANS}	RANS stress tensor	N/m^2
Ω	Rotation rate tensor	1/s
γ_M	Compressibility modification	W/m^3
$\emptyset$	Transport variable	-
φ	Wall normal stress component	-
ω	Specific dissipation rate	1/s
η	Kolmogorov length scale	m
Γ	Diffusivity	m^2/s
Δ	Filter width (element size)	m

Latin letters

Symbol	Meaning	Unit
A	Area	m^2
c_p	Specific heat capacity	J/kgK
C	Model coefficient in chapter 2	-
C	Dimensionless concentration in chapter 3-6	-
C_m	Mass flow center coordinate	m
D	Jet nozzle diameter	m
E	Total energy per unit mass	J/kg
f	Model function	-
F_b	Body force per volume	N/m^3
g	Gravitational vector	m/s^2
G_b	Buoyancy production	W/m^3
G_k	Production due to shear	W/m^3
G_ω	Production of specific dissipation	W/m^3
$G_{\omega c}$	Cross diffusion	W/m^3
G_a	Increment of wall dissipation rate	W/m^3
H	Specific enthalpy	J/kg
H_{static}	Static enthalpy	J/kg
$\mathbf{I}$	Identity matrix	-
k	Turbulent kinetic energy	m^2/s^2
l_t	Turbulent length scale	m
L	Characteristic length	m
p	Instantaneous pressure	Pa
P	Production term	W/m^3
Pr_t	Turbulent Prandtl number	-
$\dot{q}$	Heat flux	W/m^2
Q	Q value in Q-criterion	1/s^2
R	Specific gas constant	J/molK
R_u	JIC velocity ratio	-
Re	Reynold number	-
$\mathbf{S}$	Strain rate tensor	1/s
S_w	Deformation parameter	1/s
Sc	Schmidt number	-
t	Time	s
t_t	Turbulent time scale	s
t_{te}	Large eddy time scale	s
T	Temperature	K
T_c	Temperature of near-wall cell	K
u^+	Dimensionless tangential velocity component	-
U	Mean velocity in x direction	m/s
$\mathbf{W}$	Vorticity tensor	1/s
y	Wall distance	m

Superscript

Symbol	Meaning
$\bar{\emptyset}$	Mean value
$\emptyset'$	Fluctuating value
$\emptyset^T$	Matrix transpose
$\emptyset''$	Sub filtered value
$\tilde{\phi}$	Filtered value
ϕ^+	Dimensionless value
$\hat{\phi}$	RANS average value

Subscript

Symbol	Meaning
$cross$	Crossflow
i, j, k	Cartesian coordinate direction on x, y, z axis
jet	Jet nozzle
LAG	Lag EB model
SGS	Subgrid scale
SST	SST model
t	Turbulent properties
w	Wall properties

Contents

1. Introduction ... 1
  1.1 Background ... 1
  1.2 Siemens Energy AB and gas turbines ... 3
    1.2.1 The Siemens SGT-800 and 3rd generation DLE burner ... 4
    1.2.2 The Siemens SGT-750 and 4th generation DLE burner ... 4
  1.3 Problem formulation ... 5
  1.4 Objectives ... 5
  1.5 Limitations ... 6
  1.6 Thesis outline ... 6
2. Theoretical background ... 7
  2.1 Siemens STAR-CCM+ ... 7
  2.2 Governing transport equations ... 7
    2.2.1 Mass transport modelling ... 7
    2.2.2 Momentum transport modelling ... 8
    2.2.3 Energy transport modelling ... 8
    2.2.4 Equation of state ... 9
  2.3 Modelling turbulence ... 9
    2.3.1 RANS turbulence models ... 9
    2.3.2 Large eddy simulation ... 14
    2.3.3 Turbulence wall treatment ... 16
  2.4 Analysis of turbulent flow structures ... 17
  2.5 Turbulent mixing and passive scalar ... 17
3. Methodology ... 19
  3.1 Numerical set up ... 19
    3.2.1 Geometrical domain ... 19
    3.2.2 Boundary conditions ... 20
    3.2.3 Computational mesh ... 21
    3.2.4 Model formulation ... 23
    3.2.5 Analysis of results ... 24
    3.2.6 Transient simulation guidelines ... 25
  3.3 Adaptive meshing ... 27
  3.4 Previously used mesh strategies ... 28
    3.4.1 Previously used mesh strategies and realizable k-epsilon ... 28
    3.4.2 Previously used mesh strategies and LES ... 30
    3.4.3 Grid sensitivity test ... 32
4. Results and discussions ... 34
  4.1 Mesh optimization approach ... 34
    4.1.1 Optimized mesh and realizable k-epsilon model ... 36
    4.1.2 Optimized mesh and LES model ... 38
    4.1.3 Turbulence model dependence ... 40
  4.2 Additional investigation ... 41
    4.2.1 Turbulent flow analysis ... 41
    4.2.2 Dependency on turbulent Schmidt number ... 42

5. Conclusion 44
6. Future work 45
References 46
Appendices 49
  A. JIC experimental set up 49
  B. Previously used mesh strategies 50
    B1. Mesh strategies in details 50
    B2. Grid sensitivity test of mesh C3 and C4 51
  C. Turbulence model dependence of the optimized mesh 52

1. Introduction

This chapter comprises a brief background of gas turbines and how Siemens Energy AB has been enhancing overall efficiency to meet requirement of environmental aspects with the technology available today. Thereafter, problem formulation, objectives, as well as study limitations are presented. Afterward, thesis outline is provided.

1.1 Background

Gas turbines are considered as significant parts of energy production worldwide. This is due to high compatibility with wind or solar power, also high load of flexibility and fast startup practice [2]. With the growth of energy demand nowadays, environmental concern of greenhouse gases emission such as CO_2 from gas turbines has been increasing in attention, as well as traditional emission restrictions for NO_x and CO. Since NOx emission can be lowered by decreasing the local maximum temperature which results from a good premixing of air and fuel, premixed combustion thus has crucial role to mitigate pollutant emissions [3]. However, the prediction of premixed combustion is complex which means the flame behavior in the combustor system needs to be understood.

Siemens Energy AB in Finspång has been producing a wide range of gas turbines for power generation purpose. The efficiency of gas turbines has been improving by Computer Aided Engineering (CAE) technology. Computational Fluid Dynamics (CFD) is considered as a powerful development tool for gas turbines design assessment prior to the high-cost combustion engine test is performed. This leads to good insight of flow and temperature distribution which enhance thermal efficiency and lower pollutant emissions [4]. One of the most recognized software for CFD simulation is Siemens PLM's STAR-CCM+.

In order to achieve desirable low NOx emission, premixed fuel-air mixture is aimed for in the particular gas turbines. There are several geometrical parameters which may affect the premixing performance. This includes diameter and distribution of the fuel holes on the fuel pins located in the main channels of the combustor, illustrated in Figure 1 [5]. In the recent days, CFD simulation can be applied to gas turbines to predict optimal location of fuel holes by using for example Design Manager in Star-CCM+. However, careful simulation set up from preprocessing to postprocessing steps is required. A preprocessing step for computational flow field simulation called mesh generation has been considered as an important parameter which affect solution convergence and accuracy [6]. Thus, quality of the grid in the simulation is significant to be optimized.

Since an appropriate design of the mixing process is crucial for a stable low NOx emission system, reliable predictive tools are demanded. In gas turbine burners, fuel is injected to the air resulting in a partially premix of fuel and air before entering the combustion chamber which resembles to jet in crossflow (JIC). JIC is known as a simple turbulent flow and mixing configuration for studying a good fuel-air mixing ability throughout a small distance and has been favored by gas turbines industries. It has been applied to premix burner technology to capture formation of turbulent vortices and complex flow structures [1]. The phenomena related to JIC is demonstrated in Figure 2. Thus, this thesis applied a typical jet in crossflow configuration to simplify the mixing of fuel and air in gas turbines related to fuel injection nozzles at the burner in order to optimize the mesh for the future computational simulation.

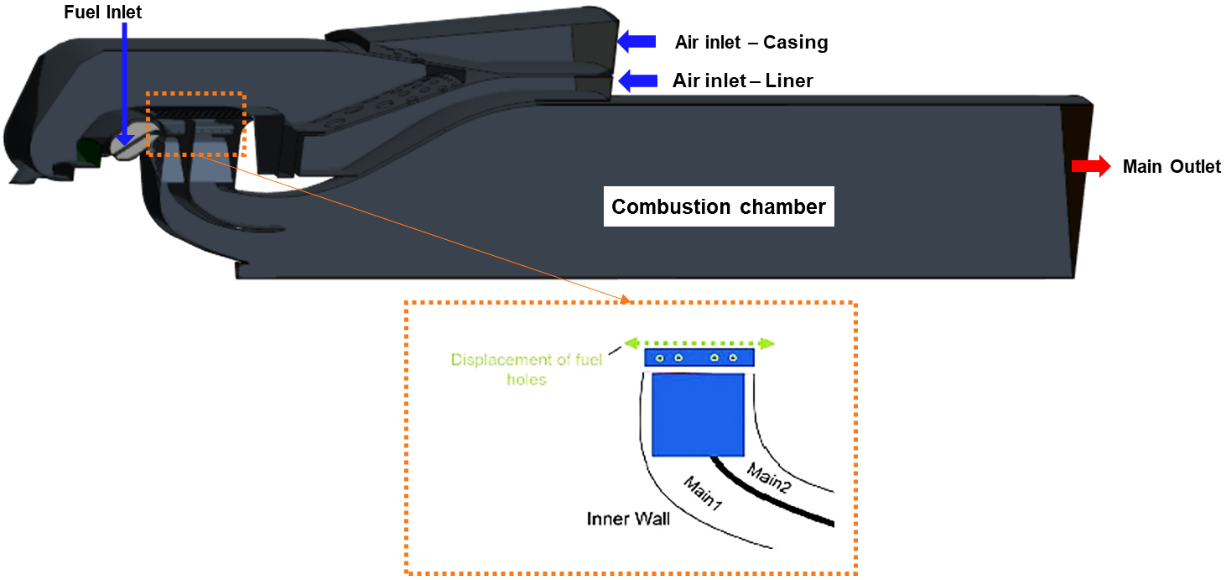

Figure 1. Siemens gas turbine SGT-750 45-degree sector model (with fuel hole displacement) [5].

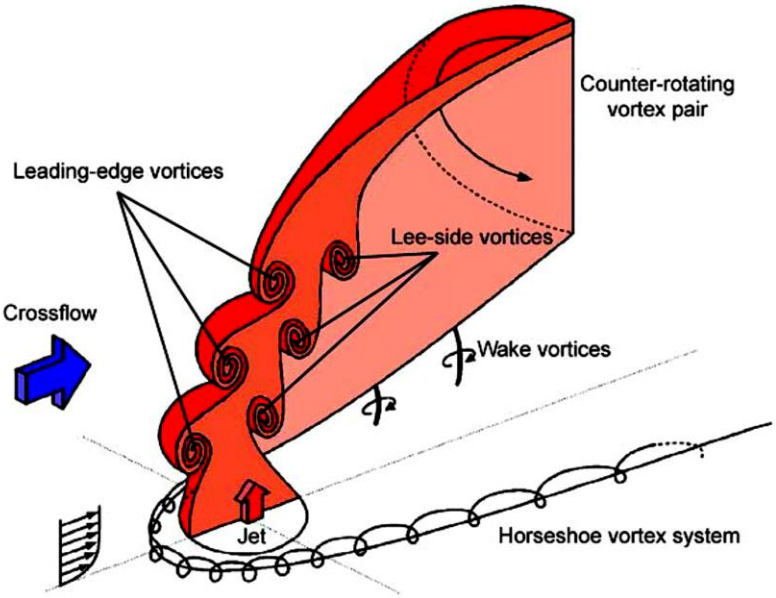

Figure 2. Jet in crossflow phenomenology [1].

1.2 Siemens Energy AB and gas turbines

A gas turbine is a kind of internal combustion engine which can be applied as a weight-efficient powerplant for the purpose to generate huge amount of electrical energy. Gas turbines use the principle of thermodynamic, Brayton cycle as shown in Figure 3. Gas turbines consist of a compressor, combustion chamber and turbine from upstream to downstream, respectively shown in Figure 4. The concept is to achieve higher inlet pressure than outlet pressure to generate useful work for electrical production. Firstly, air is fed to a compressor to increase the pressure. Air then enters combustion chamber mixed with the injected fuel. The resulting mixture is ignited in the combustion chamber and due to the exothermic chemical reactions, heat is produced. High pressure and temperature flue gases then enter the turbine part which generates power [7].

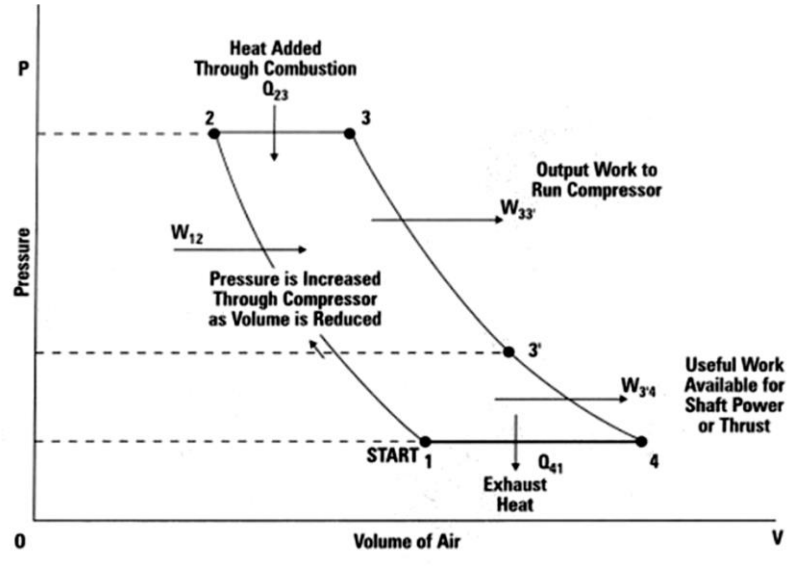

Figure 3. Brayton cycle P-V diagram showing work (W) and heat (Q) input and output [8].

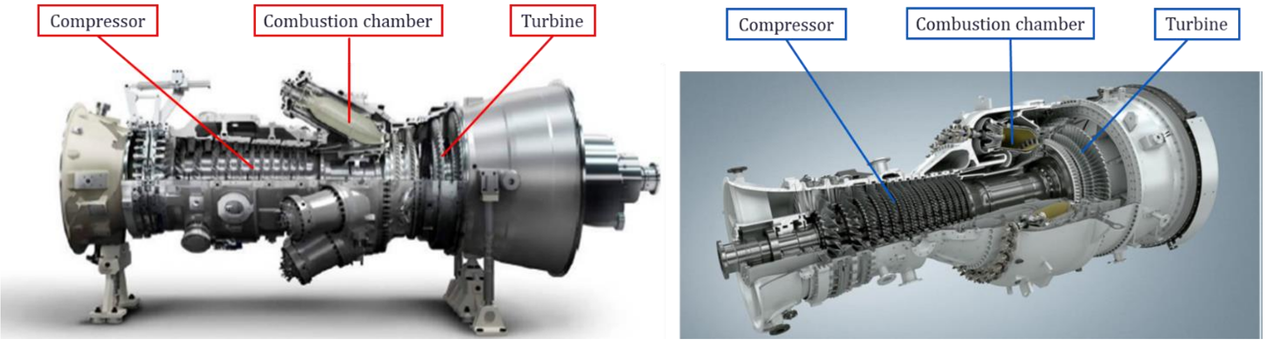

Figure 4. Gas turbine components (left) SGT-750 (right) SGT-800 [9].

The combustion chamber has been the most complicated part for gas turbines design since it consists of complex flow and the combustion environment needs to be controlled to meet the requirement of low pollutant emissions.

The dry low emission (DLE) combustor was developed in 1990s after the concept of wet low emission (WLE) to avoid using water or steam injection to cool down the flame region. The purpose of the DLE combustor is to let air and fuel premix before entering combustion chamber to have lean mixture resulting in lower local flame temperature and reduction of NOx emission. Thus, most of the fuel is burned with an excess of air [7].

1.2.1 The Siemens SGT-800 and 3rd generation DLE burner

The SGT-800 is a single shaft turbine with 15-stage axial compressor. It composes of an annular combustion chamber with 30 3rd generation DLE burners shown in Figure 5. Each burner approximately composes of 40 fuel injection nozzles in swirler generator part which can be observed from four quatrocones. It is suitable for combined heat and power generation and NOx are kept lower than 15 ppm [10].

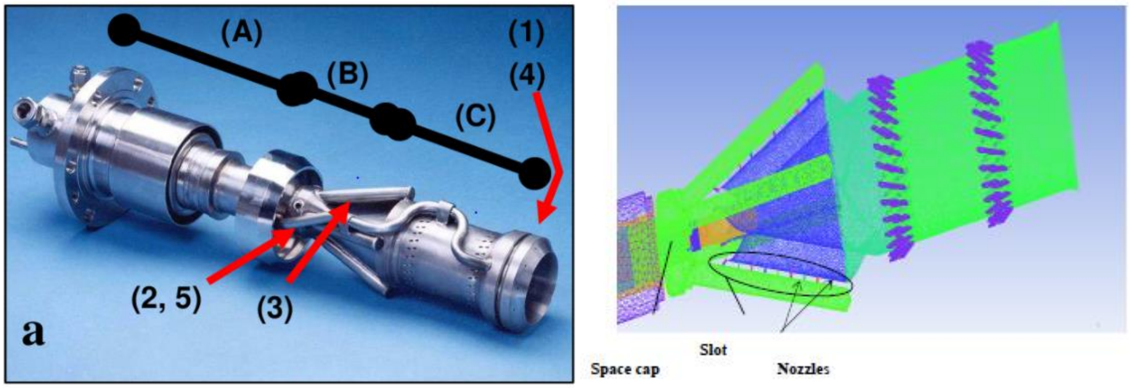

Figure 5. SGT-800 burner showing the section (A) fuel transfer (B) swirling generator (C) mixing zone with the fuel injection locations (1) pilot gas (2) central gas (3) main gas (4) pilot liquid (5) main liquid [11, 12].

1.2.2 The Siemens SGT-750 and 4th generation DLE burner

The SGT-750 is a two-shaft gas turbine and 13-stage axial compressor which is developed to be a low-weight industrial gas turbine with multiple combustion chambers. Thus, it has advantage of easy access and maintenance. A cross-section of the SGT-750 gas turbines is illustrated in Figure 6. The fuel is injected and premixed with air in main 1 and main 2 channels prior to the ignition in the combustion chamber. In order to stabilize the flame, a Rich Pilot Lean (RPL) burner is located prior the combustion chamber and has an important role acting like a small torch to ignite pilot and main flames. Moreover, swirling vanes are also included in order to generate recirculating region bounded by the quarl, to keep the velocity low for the purpose of flame stabilization. A transition duct is also placed at the end of the chamber to ensure the cooling process for the whole system [13].The 4th generation burner has been designed for extremely low NOx emission lower than 15 ppm by further optimizing aerodynamic and fuel-air mixing. Thus, the system of SGT-750 is operated in lean premixed combustion mode.

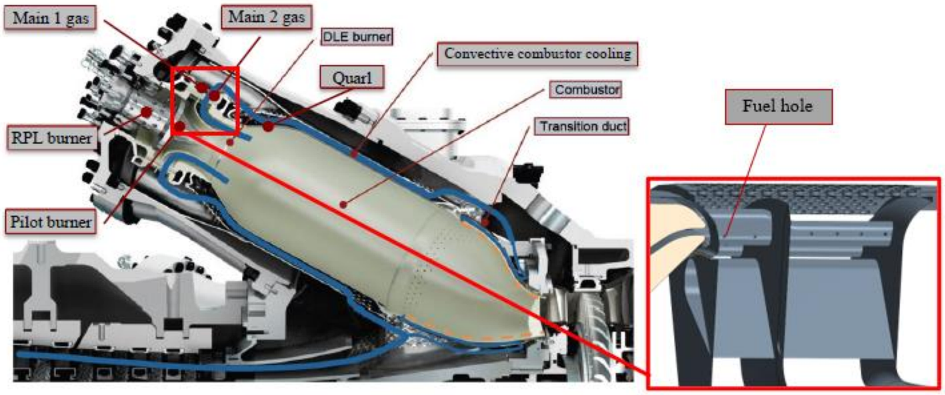

Figure 6. Cross-section of SGT 750 combustion Chamber and fuel holes [14].

1.3 Problem formulation

Due to environmental concern on gas turbines, pollutant emissions generated should be as low as possible. In order to reduce NOx emissions while increasing the performance of the gas turbines themselves, the flame behavior in combustor environment needs to be well investigated. Lean premixed combustion is aimed for the lower flame temperature, thus decreasing NOx emissions according to the concept of DLE combustor. The performance can be affected by the location and distribution of the fuel holes on the fuel pins which can be optimized using Computational Aided Engineer (CAE) concept in the design process. In this thesis, Siemens PLM's STAR-CCM+ was chosen as a software to study the complex behavior of the flow. Meshing strategy was extensively studied since it can highly affect the solution convergence and accuracy. Jet in Crossflow (JIC) configuration obtained from the previous study of Siemens Energy in collaboration with Karlsruhe Institute of Technology, Germany [1] was used to simplify the fuel injection nozzles at the burners. Previously used mesh strategies in SGT- 750, SGT-800 and other projects were investigated in terms of grid independence properties and accuracy by validation to the experimental data obtained from F. Galeazzo et al,2010 [1]. The main goal is to further optimize and confirm grid indenpendece of the new mesh strategy in order to achieve higher accuracy with least number of cells, so the optimized mesh can be further applied in CFD simulation of fuel hole distribution in the gas turbines.

1.4 Objectives

- To estimate the accuracy of the previously used mesh strategies around the nozzle region applied in previous projects (e.g. SGT-750 and SGT-800) using 'Jet in Crossflow' as simplified case where experimental data is available for validation.
- To improve and optimize the mesh for best balance between cost-efficiency and accuracy of the fuel nozzle and downstream mixing resolution.
- To investigate grid dependency of the optimized mesh strategy.
- To evaluate performance of optimized mesh strategy using different turbulence models.
- To provide mesh recommendation for future computational simulation.

1.5 Limitations

The restrictions of this thesis are as follows,

- Air with isothermal condition is used for the whole domain. This might lead to a deviation of the results and when the optimized mesh strategy is further applied to the actual gas turbines simulation.
- Jet in Crossflow (JIC) configuration and boundary conditions from F. Galeazzo et al,2010 [1] are applied to all case studies. The actual gas turbines configuration also inlet, outlet and operating conditions might not be the same as the study. Thus, the jet trajectory may deviate from the results. However, one can further apply the optimized mesh strategy and suitably adjust to actual cases.
- Realizable k-epsilon and Lag Elliptic Blending turbulence models are performed at steady state condition which can affect the results since the mixing is transient in nature.

1.6 Thesis outline

The thesis report begins with a theoretical background which provides relevant theories required for more understanding of the thesis, mostly CFD aspects. Later, methodology including JIC geometrical configuration, meshing simplification concept, previously used mesh strategies details and simulation set up is presented. Afterwards, results of the study are presented with discussions to deeply explain the outcome. Lastly, conclusions based on discussion parts and future perspectives are presented.

2. Theoretical background

In this chapter, the principle of fluid dynamics and CFD aspects are given for a better understanding of the thesis. Also, equations used throughout the thesis are also presented.

Computational fluid dynamics (CFD) is computational modeling of fluid flow problems. Fluid flow characteristics can be monitored and visualized by solving for local transport variables such as velocity, pressure, concentration and temperature in each discretized volume in the domain. In comparison to the conventional physical examination, this enables products and processes to be analyzed, tested, and optimized with greater detail and reliability. The key equations, models, and underlying assumptions used to simulate a jet in crossflow are reviewed in this chapter.

2.1 Siemens STAR-CCM+

In this study, the Siemens Simcenter STAR-CCM+ was used for the numerical analysis of turbulent mixing. It can simulate a wide variety of physical phenomena. The mathematical models that explain the physics in the software are based on fundamental conservation principles. The control volume describes a portion of space where fluid is allowed to flow, according to Eulerian implementation [15]. For an infinitely small control volume, the fundamental equations are described in differential form. However, since the total number of unknowns exceeds the number of equations, these partial differential equations cannot be solved directly. The terms must be closed in order to solve these equations. The additional turbulence equations act as supplements to solve the partial differential equations to obtain the closure. After that, the program used discretization to find a solution.

2.2 Governing transport equations

The simulation of a jet in crossflow is primarily concerned with three aspects of modeling: mass, momentum, and energy transport in the domain. For these three aspects, three fundamental transport equations derived from the theory of mass, momentum, and energy conservation [15] [16] are solved. All of these equations are based on four major transport variables: density, velocity, pressure, and temperature (ρ, v, p, T).

2.2.1 Mass transport modelling

The mass transport equation, also known as the continuity equation, is given by Equation (1). The density (ρ) or mass per unit volume is applied to model the mass. The convection of mass in to or out of the system with the continuum velocity (v) is represented by the second term in the equation.

$$\frac{\partial \rho}{\partial t} + \nabla \cdot (\rho v) = 0 \tag{1}$$

2.2.2 Momentum transport modelling

Conservation of momentum is derived from Newton's law of motion and is much more difficult to deal with opposed to mass and energy transport modelling. This is due to the fact that momentum is a vector quantity in both magnitude and direction, implying that momentum must be conserved in all directions. Momentum transport modelling is governed by Navier-Stokes equation which includes linear and angular momentum.

$$\frac{\partial(\rho v)}{\partial t} + \nabla \cdot (\rho v \otimes v) = -\nabla \cdot (p\mathbf{I}) + \nabla \cdot \tau + F_b \qquad (2)$$

Here, $\otimes$ is the outer product. Equation (2) includes the effect of convection, pressure gradient, viscous stress and resultant body forces. Collectively, the term pressure gradient and diffusion constitute stress tensor (σ) as shown in Equation (3).

$$\sigma = -(p\mathbf{I}) + \tau \qquad (3)$$

According to the symmetry of the stress tensor in Equation (4), conservation of angular momentum is then achieved.

$$\sigma = \sigma^T \qquad (4)$$

2.2.3 Energy transport modelling

Energy transport modelling obtained from first law of thermodynamics is used to govern thermodynamics in the domain system. Equation (5) shows how the total energy per unit mass varies over time according to convection, heat flux, viscous force and resultant body forces, respectively.

$$\frac{\partial(\rho E)}{\partial t} + \nabla \cdot \big((\rho E + p)v\big) = -\nabla \cdot \dot{q} + \nabla \cdot (\tau \cdot v) + F_b \cdot v \qquad (5)$$

Enthalpy (H) of the system is constituted by variables in the second term including energy and pressure. In Equation (6), enthalpy is defined as summation of two different terms, static enthalpy (H_{static}) and kinetic energy ($\frac{|v|^2}{2}$).

$$\rho E = \rho H - p = \rho\left(H_{static} + \frac{|v|^2}{2}\right) - p \qquad (6)$$

For the simplification of ideal gas, H_{static} can be written as product of specific heat capacity (c_p) and temperature as shown in Equation (7).

$$H_{static} = c_p T \qquad (7)$$

2.2.4 Equation of state

In order to close the equation system generated by mass, momentum and energy conservation in Equation (1), (2) and (5), an equation of state is applied. Equation of ideal gas where intermolecular forces are neglected is introduced to simplify the equation system.

$$p = \rho R T \tag{8}$$

In total, there are 6 equations to be solved for 6 unknown dependent variables. Thus, the system is closed.

2.3 Modelling turbulence

Most flows in nature and engineering are turbulent, which is a phenomenon characterized by irregularities in flow patterns caused by instabilities at high flow rates. Even at low velocity, the flow of a fluid with low kinematic viscosity as air is likely to be turbulent. Turbulence is a complex state of fluid flow characterized by random fluctuations that can be both advantageous and problematic. In a combustion chamber of the gas turbines, turbulence is beneficial for fuel and air mixing. However, on the other hand, it can result in efficiency losses. For more understanding, characteristics of general turbulence are summarized below,

- Irregular, random and chaotic flow
- Broad spectrum of eddies, swirling flow structures leading to wide range of velocity, time and length scales
- High diffusive transport which allows the faster mixing rates of mass, momentum and energy
- Instability at high Reynold number (Re)
- Intrinsically three-dimensional structures due to vortex stretching
- Transport of turbulent kinetic energy from largest scales to smallest scales and further dissipation into heat, i.e. the so called energy cascade

In order to describe the flow regime, Reynold number (Re) is used. Turbulent flow are likely to occur at high Reynolds number at which inertial forces dominate over viscous forces. Energy is transferred to smaller scale eddies which finally dissipate kinetic energy into heat [16].

2.3.1 RANS turbulence models

Turbulence complicates the flow behavior by causing stochastic motion, which is described as high frequency irregular fluctuations of the transport quantities. This implies that solving the flow directly in a small scale would be costly due to the large computational resources needed, which is referred to as Direct Numerical Simulation (DNS). To prevent this, turbulence is instead simulated using physics-based turbulence models. The Reynolds-Averaged Navier-Stokes (RANS) model is the most common and least expensive model, in which stochastic quantities are not directly solved but averaged transport quantities are solved for instead. Thus, additional models are required for the closure of the averaged equations. RANS modelling is therefore considered as an effective way to eliminate high-cost turbulent fluctuation, but robust predictions can still be obtained.

Reynolds decomposition is defined as decomposing instantaneous transport variables (ϕ) to two separated parts: average component ($\bar{\phi}$) and fluctuating component (ϕ'). The transport equations are averaged in order to eliminate the fluctuating components. Moreover, a new Reynold stress tensor denoted as τ_{RANS} is added which makes the terms $\nabla \cdot \tau$ in Equation (2) and (5) for momentum and energy conservation become $\nabla \cdot (\bar{\tau} + \tau_{RANS})$.

Eddy viscosity model can be applied to close τ_{RANS} . It states τ_{RANS} is directly related to mean strain rate tensor ($\bar{\boldsymbol{S}}$) and turbulent viscosity (μ_t) obtained from Boussinesq approximation.

$$\tau_{RANS} = 2\mu_t \bar{\boldsymbol{S}} - \frac{2}{3}\mu_t (\nabla \cdot \bar{v})\mathbf{I} \tag{9}$$

$$\bar{\boldsymbol{S}} = \frac{1}{2}(\nabla\bar{v} + (\nabla\bar{v})^T) \tag{10}$$

μ_t can be estimated as a function of two turbulence transport quantities: turbulent velocity and length scale. Thus, two additional equations are needed. Compared to other modelling alternative, the reynold stress transport (RST) require more equations due to the modelling method that solves each variable in τ_{RANS} separately. According to this, eddy viscosity based models are more common in industrial application and they are chosen for the thesis study.

2.3.1.1 Realizable k-epsilon model

The k-epsilon model has been regarded as the most robust model used in industry. It has been proven reasonably accurate and reliable. Since, the model has been developed and modified for decades, various changes of the model have been made. According to the studies [17] [18], the interaction within fluctuating velocity component can appear negative at high strain rate. For the problem to be solved, turbulent dissipation rate (ε) and model coefficient (C_μ) are revised. Realizable k-epsilon turbulence model was developed which typically provides more reasonable solution and more accurate result than standard k-epsilon model. Thus, the realizable k-epsilon model was chosen as performed model in the study.

For the realizable k-epsilon model, μ_t is modelled as a function of turbulent kinetic energy (k) and turbulent dissipation rate (ε) with the relation of turbulent time scale (t_t) as shown in Equation (11) and (12).

$$\mu_t = \rho k C_\mu f_\mu t_t \tag{11}$$

$$t_t = t_{te} = \frac{k}{\varepsilon} \tag{12}$$

Here, the turbulent time scale (t_t) is equivalent to large eddy time scale (t_{te}) for simplification. Two additional transport equations are required in order to solve k and ε. Equation (13) and (14) describe the terms of accumulation, convection by average velocity, molecular diffusion, turbulent diffusion, production and dissipation rate.

$$\frac{\partial(\rho k)}{\partial t} + \nabla \cdot (\rho \bar{v} k) = \nabla \cdot \left[\left(\mu + \frac{\mu_t}{C_{\sigma k}}\right)\nabla k\right] + (P_k - \gamma_M) - \rho\varepsilon \tag{13}$$

$$\frac{\partial(\rho \varepsilon)}{\partial t} + \nabla \cdot (\rho \bar{v} \varepsilon) = \nabla \cdot \left[\left(\mu + \frac{\mu_t}{C_{\sigma \varepsilon}}\right)\nabla \varepsilon\right] + \frac{1}{t_{te}} C_{\varepsilon 1} P_\varepsilon - C_{\varepsilon 2} f_2 \rho \left(\frac{\varepsilon}{t_{te}}\right) \tag{14}$$

Here, P denotes production term. P_k constitutes of shear induced turbulence production (G_k) and buoyancy induced turbulence production (G_b) while P_ε includes the production of strain rate ($\bar{\boldsymbol{S}}$) and buoyancy. Note that, the term G_k is not included in P_ε to unphysical negative value in sink term. In addition, the term γ_M denotes compressibility effect in k production.

$$P_k = G_k + G_b \tag{15}$$

$$P_\varepsilon = |\bar{\boldsymbol{S}}|k + C_{\varepsilon 3} G_b \tag{16}$$

$$G_k = \mu_t |\bar{\boldsymbol{S}}|^2 - \frac{2}{3}\rho k \nabla \cdot \bar{v} - \frac{2}{3}\mu_t (\nabla \cdot \bar{v})^2 \tag{17}$$

$$G_b = \frac{\beta \mu_t}{Pr_t} \nabla \bar{T} \cdot g \tag{18}$$

$$\text{where, } \beta = -\frac{1}{\rho}\frac{\partial \rho}{\partial \bar{T}} \text{ for ideal gas} \tag{19}$$

$$\gamma_M = \frac{\rho C_M k \varepsilon}{{v_c}^2} \tag{20}$$

For clarification, Pr_t, g, v_c terms represent the turbulent Prandtl number of turbulent, gravitational variable and velocity of sound, respectively.

The k-epsilon turbulence model usually takes two-layer approach near-wall modelling into account. This is beneficial to the simulation since the flow environment can be solved up to viscous affected layer near the wall boundary. This approach separates the simulation domain into bulk region and near-wall layer where turbulent viscosity at near-wall layer is assigned to wall distance Reynolds number (Re_w) . A function of wall proximity indicator (f_w) is also added to μ_t equation.

$$\mu_t = f_w \mu_{t,bulk} + (1 - f_w)\mu_{t,near-wall} \tag{21}$$

$$\mu_{t,near-wall} = 0.42 \mu Re_w {C_\mu}^{1/4} \left[1 - \exp\left(\frac{-Re_w}{70}\right)\right] \tag{22}$$

$$Re_w = \frac{\rho \sqrt{k} y}{\mu} \tag{23}$$

2.3.1.2 Lag EB k-epsilon model

The lag elliptic blending (Lag EB) turbulence model is developed to lower the Re dependency in standard k-epsilon model and takes into account the lag feature. Additional terms describing the increment of near-wall dissipation rate and redistribution of wall-normal velocity fluctuations are added to ε transport equations [19]. Moreover, over-prediction of turbulent kinetic energy is also avoided by adding a new production term related to stress-strain lag. Thus, the model has benefits in simulating separated and unsteady flow with large streamline curvature. According to this, lag EB turbulence model has been chosen as the model in the study.

For the governing equations, the terms $C_{\mu LAG}, C_{tLAG}, t_{tLAG}$ are added for modification which are depicted in Equation (24) and (25). Turbulence anisotropy near the wall is accounted in the model through wall normal stress component denoted as φ.

$$\mu_t = \rho k C_{\mu LAG} \varphi \left[\min\left(t_{tLAG}, \frac{1}{\sqrt{3} C_{\mu LAG} \varphi |\bar{\boldsymbol{S}}|} \right) \right] \tag{24}$$

$$t_{tLAG} = \sqrt{{t_{te}}^2 + {C_{tLAG}}^2 \frac{\upsilon}{\varepsilon}} \tag{25}$$

Therefore, the transport equation of φ must be solved as well as the k and ε transport equations. In addition, the term ε is defined as dissipation rate of homogeneous mixture to lower Re independency affect in the model. The transport equations of k, ε and φ are shown in Equations (26)-(28).

$$\frac{\partial(\rho k)}{\partial t} + \nabla \cdot (\rho \bar{v} k) = \nabla \cdot \left[\left(\frac{\mu}{2} + \frac{\mu_t}{C_{\sigma k}} \right) \nabla k \right] + (P_k - \gamma_M) - \rho \varepsilon \tag{26}$$

$$\frac{\partial(\rho \varepsilon)}{\partial t} + \nabla \cdot (\rho \bar{v} \varepsilon) = \nabla \cdot \left[\left(\frac{\mu}{2} + \frac{\mu_t}{C_{\sigma \varepsilon}} \right) \nabla \varepsilon \right] + \frac{1}{t_{te}} C_{\varepsilon 1 LAG} P_{\varepsilon LAG} - C_{\varepsilon 2} \rho \left(\frac{\varepsilon}{t_{te}} \right) \tag{27}$$

$$\frac{\partial(\rho \varphi)}{\partial t} + \nabla \cdot (\rho \bar{v} \varphi) = \nabla \cdot \left[\left(\frac{\mu}{2} + \frac{\mu_t}{C_{\sigma \varphi}} \right) \nabla \varphi \right] + P_{\varphi} \tag{28}$$

To clarify the production term in each equation, $P_{\varepsilon LAG}$ in ε transport equations has been modified by including shear induced turbulence production (G_k) and additional term G_a accounted for increment of near wall dissipation rate. The term G_a includes a blending factor (α) in order to add near wall effect to lag EB model. Moreover, the terms f_w and f_h are also included in P_{φ}. These two factors account for allocation of wall-normal velocity variation, also pressure variation from the wall. This makes lag EB model suitable for anisotropic turbulence and kinematic blocking due to wall.

$$P_{\varepsilon LAG} = C_{\varepsilon 3} G_b + G_k + \frac{1}{C_{\varepsilon 1 LAG}} G_a \tag{29}$$

$$P_{\varphi} = -(2 - C_{\varepsilon 1 LAG}) \frac{\varphi}{k} (G_k + G_b) + \rho (1 - \alpha^3) f_w + \rho \alpha^3 f_h \tag{30}$$

$$G_a = C_k(1-\alpha)^3 \upsilon \mu_t \frac{k}{\varepsilon}[\nabla \cdot |2\overline{\boldsymbol{S}}n|n]^2 \tag{31}$$

$$\nabla \cdot \left({l_t}^2 \nabla \alpha\right) = \alpha - 1 \tag{32}$$

$$l_t = C_L \sqrt{\frac{k^3}{\varepsilon^3} + {C_\eta}^2 \sqrt{\frac{\upsilon^3}{\varepsilon}}} \tag{33}$$

Here n denotes wall normal direction and l_t denotes turbulent length scale.

2.3.1.3 SST k-omega model

The shear stress transport (SST) k-omega turbulence model solves for the specific dissipation rate (ω) in order to avoid the problem of modelling ε in the near wall region. This enables SST k-omega model to solve the flow throughout near wall layer and specific wall function is not required. Due to this, the SST model allows solving the flow in the near wall region subjected to adverse gradient with high accuracy. SST k-omega model involves two transport equations i.e. one for turbulent kinetic energy and one equation for the specific dissipation rate and has been developed to avoid the high sensitivity to ω in free stream and inlet boundary condition [20]. By this reason, SST model has been selected to be one of the turbulence models in the thesis.

For SST modelling, governing equation include turbulent viscosity which is modelled by SST turbulent time scale (t_{tSST}) where the term f_2 is included in order to account for the wall distance (y).

$$\mu_t = \rho k t_{tSST} \tag{34}$$

$$t_{tSST} = \min\left(\frac{1}{\omega}, \frac{C_{\alpha 1}}{|\overline{\mathbf{W}}| f_2}\right) \tag{35}$$

$$f_2 = \tanh\left(\left(\max\left(\frac{2\sqrt{k}}{C_{\omega 1}\omega y}, \frac{500\upsilon}{y^2 \omega}\right)\right)^2\right) \tag{36}$$

Governing equations for k and ω are shown in Equations (37) and (38).

$$\frac{\partial(\rho k)}{\partial t} + \nabla \cdot (\rho \bar{v} k) = \nabla \cdot [(\mu + C_{\sigma k SST}\mu_t)\nabla k] + P_k - \rho C_{\omega 1}\omega k \tag{37}$$

$$\frac{\partial(\rho \omega)}{\partial t} + \nabla \cdot (\rho \bar{v} \omega) = \nabla \cdot [(\mu + C_{\sigma\omega}\mu_t)\nabla \omega] + P_\omega - C_{\omega 2}\omega^2 \tag{38}$$

Here the term P_ω is a summation of production of specific dissipation rate denoted as G_ω and cross diffusion term assigned as $G_{\omega c}$ and described in Equations (39)-(41).

$$P_{\omega} = G_{\omega} + G_{\omega c} \tag{39}$$

$$G_{\omega} = \rho C_{\gamma}\left[\left(|\bar{\boldsymbol{S}}|^{2} - \frac{2}{3}(\nabla \cdot \bar{v})^{2}\right) - \frac{2}{3}\omega\nabla \cdot \bar{v}\right] \tag{40}$$

$$G_{\omega c} = 2\rho(1 - f_1)\, C_{\sigma\omega c}\frac{1}{\omega}\nabla k \cdot \nabla\omega \tag{41}$$

In Equation (41), the blending function f_1 has an important role for the cooperation of k-epsilon and k-omega models. It can be explained that f_1 is increased within the near-wall region resulting in reduction of $G_{\omega c}$ in SST model which means that the model is now simplified to standard k-omega model. On the other hand, further away from the wall, f_1 is reduced so that the impact of $G_{\omega c}$ in ω transport equation gets larger making the model similar to that of the k-epsilon model.

2.3.2 Large eddy simulation

Large Eddy Simulation (LES) is a turbulence model that compared to RANS models requires more computational resources, however, compared to DNS it significantly reduces the computational costs by modelling the smallest length scales in the flow environment, which would otherwise consume the majority of the computational resources. This is done by introducing low pass filtering which filters out the small eddies by the specified filter width. In a LES model, sub-grid scale models are applied to model the smallest eddies while large eddies are resolved as shown in Figure 7 . However, this filtering technique decreases the model's accuracy, especially in near-wall region. Since LES does not use time averaged value of transport variables, the simulation is always required to perform in unsteady mode.

In order to ensure that all large eddies can be captured as well as small eddies can be modelled, the computational grid which is considered as the simplest filtering method is taken into account. According to LES recommendations [16], Kolmogorov length scale (η) and Taylor microscale (λ) are applied. These scales indicate the proper cell size that should be applied for LES simulation in order to model eddies down to inertial range. Thus, the reasonable cell size (Δ) to be applied for the filtering in LES simulation can be concluded as $\eta<\Delta<\lambda$ and $\Delta\approx\lambda$. These two length scales are shown in Equations (42) and (43).

$$\eta = \left(\frac{\upsilon^{3}}{\varepsilon^{4}}\right)^{\frac{1}{4}} \tag{42}$$

$$\lambda \approx \left(\frac{10\upsilon k}{\varepsilon}\right)^{\frac{1}{2}} \tag{43}$$

The instantaneous transport variables are decomposed into filtered component ($\widetilde{\phi}$) and sub filtered component (ϕ''). By inserting the decomposed transport variables into Navier Strokes equations, model equations are given by Equations (44)-(46). It can be observed that the stress tensor terms become the combination of filtered component and subgrid scale part.

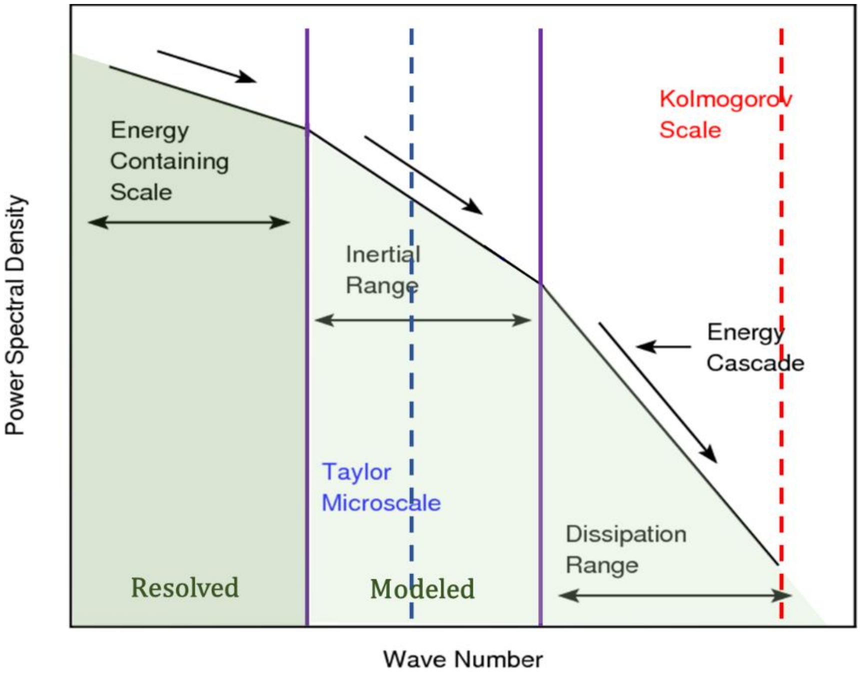

Figure 7. LES filtering [21].

$$\frac{\partial \rho}{\partial t} + \nabla \cdot (\rho \tilde{v}) = 0 \tag{44}$$

$$\frac{\partial (\rho \tilde{v})}{\partial t} + \nabla \cdot (\rho \tilde{v} \otimes \tilde{v}) = -\nabla \cdot (\tilde{p}\mathbf{I}) + \nabla \cdot (\tilde{\tau} + \tau_{SGS}) + F_b \tag{45}$$

$$\frac{\partial (\rho \tilde{E})}{\partial t} + \nabla \cdot \left((\rho \tilde{E} + \tilde{p}) \tilde{v} \right) = -\nabla \cdot \dot{\tilde{q}} + \nabla \cdot ((\tilde{\tau} + \tau_{SGS}) \cdot \tilde{v}) + F_b \cdot \tilde{v} \tag{46}$$

$$\tau_{SGS} = 2\mu_{tSGS}\mathbf{S} - \tfrac{2}{3}(\mu_{tSGS}\, \nabla \cdot \tilde{v})\mathbf{I} \tag{47}$$

However, the subgrid scale turbulent viscosity denoted as μ_{tSGS} is computed from subgrid scale model. In this study, the wall-adapting local-eddy viscosity (WALE) subgrid scale model is applied. The WALE subgrid scale model has been chosen since it has less sensitivity to model coefficient C_w. It solves the problem that C_w is not constant but it depends on the flow conditions. Thus, for the WALE subgrid scale model, turbulent viscosity of unresolved eddies can be written as Equation (48).

$$\mu_{tSGS} = \rho \Delta^2 S_w \tag{48}$$

$$S_w = \frac{{\mathbf{S}_d}^{3/2}}{{\mathbf{S}_d}^{5/4} + \mathbf{S}^{5/2}} \tag{49}$$

$$\mathbf{S}_d = \frac{1}{2}[(\nabla v \cdot \nabla v) + (\nabla v \cdot \nabla v)^T] - \frac{1}{3} tr(\nabla v \cdot \nabla v)\mathbf{I} \tag{50}$$

2.3.3 Turbulence wall treatment

Modelling the turbulent flow within the near-wall region is challenging due to more complex condition of the boundary layer compared to the bulk flow. Typically, there are two main categories for near-wall modelling: effect of the wall is already included in the turbulence model and using additional wall treatment. The first approach has already been discussed with the mention of two-layer approach in k-epsilon model in section 2.3.1.1 and blending function in k-omega model in section 2.3.1.3. Although, applying these functions in turbulence models requires high computational power since the computational grid must be highly refined in order to solve the flow up to the wall region. Therefore, this section is provided to understand more about wall treatment.

Since walls can be considered as the source of vorticity, a reliable approach to solve the flow in the near-wall region is required. Wall boundary layer can be categorized into three sub-regions based on the dimensionless wall distance (y^+) and dimensionless tangential velocity component (u^+) values as shown in Figure 8. Definition of y^+ and u^+ are given in Equations (51) and (52). The first layer with y^+<5 called viscous sublayer is the layer which directly contacts to the wall and the flow is mostly dominated by viscous effect. While the buffer layer region in the zone 5< $y^+ < 30$ is a translational layer between viscous sublayer and log layer. Lastly, turbulence is dominated in the log layer.

$$y^+ = \frac{y\rho u^*}{\mu} \tag{51}$$

$$u^+ = \frac{u}{u^*} \tag{52}$$

Where u^* can be differently described according to the type of wall function. In this study, blended wall function is chosen because the function can be applied to the whole sub-region near the wall. It enables wall treatment in translational buffer region which is represented by the blending of both viscous sublayer and log layer. Hence, u^* can be written as Equation (53).

$$u^* = f_\gamma \sqrt{\frac{\mu|v_{tangential}|}{\rho y}} + (1 - f_\gamma){C_\mu}^{1/4} k^{1/2} \tag{53}$$

In Star-CCM+, four types of wall treatment are available. This includes Low-y^+, High y^+, All y^+ and Two-layer all y^+ based on y^+values of the system. Each wall treatment includes wall shear stress (τ_w) as shown in Equation (54).

$$\tau_w = |\tau_{wf}| = \left|\rho u^{*2} \frac{\hat{v}_{tangential}}{|\hat{v}_{tangential}|}\right| \tag{54}$$

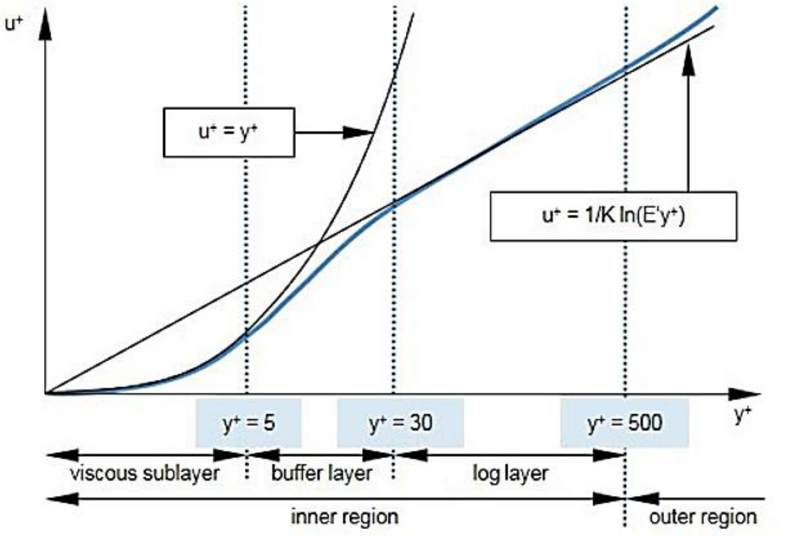

Figure 8. Boundary region of inner layers based on the plot of y+ and u+ [15].

2.4 Analysis of turbulent flow structures

In order to visualize unsteadiness of the flow structure, the vortex visualization method called Q-criterion is used [22]. This enables more understanding of flow environment in the systems such as turbulent structures. The Q-criterion is derived from decomposition of velocity gradient tensor into strain rate tensor and rotation rate tensor as shown in Equation (55).

$$\frac{\partial v_i}{\partial x_j} = S_{ij} + \Omega_{ij} = \frac{1}{2}\left(\frac{\partial v_i}{\partial x_j} + \frac{\partial v_j}{\partial x_i}\right) + \frac{1}{2}\left(\frac{\partial v_i}{\partial x_j} - \frac{\partial v_j}{\partial x_i}\right) \tag{55}$$

Q is defined as the second invariant of velocity gradient tensor as shown in Equation (56).

$$Q = \frac{1}{2}\left(\Omega_{ij}\Omega_{ij} - S_{ij}S_{ij}\right) \tag{56}$$

According to this equation, Q can be used as criterion to visualize turbulent structures in the flow. For positive Q values, $\Omega_{ij}\Omega_{ij} > S_{ij}S_{ij}$, the flow field is dominated by rotation and vorticity. The region of interest can be further visualized by generating iso surface, surface of constant value which is available in STAR-CCM+.

2.5 Turbulent mixing and passive scalar

Turbulent mixing designates the mass transport which is caused by turbulence. Generally, mixing can be classified into reactive and passive mixing [23]. Flow dynamics and properties are influenced by reactive mixing but not by passive mixing. Examples of the simplest case, the passive mixing is mixing of non-reacting species and mixing of density-related gases. In this study, passive mixing is in focus to simulate jet in crossflow environment. Passive mixing is mechanically governed by advection and molecular diffusion. Advection defines mass transport caused by flow and turbulence while molecular diffusion refers to the motions of molecular level. A passive scalar is a tracer which does not actively engage in the flow behavior but devotedly follow the fluid motion. It is presented in low concentration in the fluid flow to assist the understanding of mixing between the interacting flows.

An important dimensionless number which describes turbulent mixing is turbulent Schmidt number (Sc_t). It defines as the ratio between turbulent viscosity (υ_t) and turbulent diffusivity (Γ_t) as shown in Equation (57).

$$Sc_t = \frac{\upsilon_t}{\Gamma_t} \tag{57}$$

According to its definition, Sc_t can be used to determine the diffusion of a mixture in the mixing process. Lower Sc_t results in higher diffusivity, thus increases the mixing. Typically, the optimum values of Sc_t used in CFD calculation are widely distributed in the range of 0.5-0.9. However, it depends on local flow characteristics in each case [24].

3. Methodology

This chapter includes the overall thesis methodology and final set up for JIC and turbulent mixing simulation in STAR CCM+. It also presents parameters in consideration relating to the study and important simulation guidelines for LES turbulence model.

In the recent gas turbine burners such as SGT-750 and SGT-800, fuel is injected via fuel nozzles to be premixed with air before entering the combustion chamber where the reactions occur. The fuel-air mixing phenomena resembles to 'Jet in Crossflow' (JIC) where the jet nozzle is mounted to the wall of a crossflow channel as shown in Figure 9. This configuration allows modified geometry to capture turbulent mixing and complex turbulent flow structures. According to section 1.2*,* each gas turbine configuration includes several fuel nozzles to be investigated. However, each fuel injection nozzle can be represented by the simplified JIC to facilitate low computational cost. In this study, Siemens PLM's STAR-CCM+ computational software was used to predict turbulent flow field and investigate turbulent mixing of the JIC.

3.1 Numerical set up

Siemens PLM's STAR-CCM+ was used to solve turbulent transport equations of mass, momentum and energy. Computational boundary condition was simplified with the assumption of constant velocity profiles of crossflow and jet inlet.

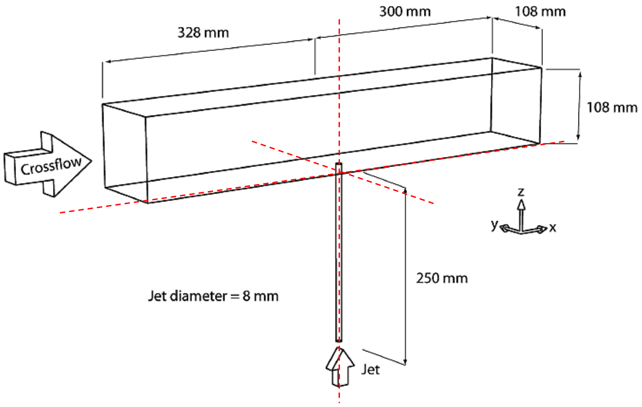

Figure 9. JIC geometrical dimensions [1].

3.2.1 Geometrical domain

The JIC configuration used in the study, illustrated in Figure 9 was replicated from the study of Siemens Energy in collaboration with Karlsruhe Institute of Technology, Germany [1]. This includes of rectangular crossflow channel and 8 mm diameter (D) long jet nozzle pipe located at 328 mm downstream from crossflow inlet matching the experimental set up. The crossflow channel was extended to 108 mm for both y and z direction with a jet nozzle length of 250 mm to allow a fully developed velocity profile. For this study, half symmetrical domain was used for steady simulation to save computational cost while the full domain was applied for implicit unsteady simulation to take into account the fluctuation effect. Note that the contraction nozzle at the beginning of the crossflow inlet regarding the experimental set up in Appendix A was not included in the computational domain. In order to clarify the axes used in the study; x denotes location in the direction of the flow from crossflow inlet to downstream, y denotes direction from the side wall and z denotes direction above nozzle injector plane.

3.2.2 Boundary conditions

The inlet of both crossflow and jet were defined as constant velocity profile as summarized in Table 1. Jet in crossflow was characterized by JIC velocity ratio denoted as R_u where R_u can be calculated by Equation (58) which includes the bulk jet velocity (U_{jet}) and maximum mean velocity in the x direction at x/D=-1.5 upstream (U_{cross}). This location was arbitrarily selected to characterize the crossflow velocity in the study [1].

$$R_u = \left(\frac{\rho_{jet} {U_{jet}}^2}{\rho_{cross} {U_{cross}}^2}\right)^{\frac{1}{2}} \tag{58}$$

The definition of R_u compensated for the difference between experimental data and literature data from the wind tunnel. Note that the crossflow velocity was not obtained from the bulk velocity but characterized by the value of U_{cross} instead. Boundary conditions used in the study were defined with the aim to obtain $R_u = 4$.

Table 1. Boundary conditions [1].

Crossflow Inlet	Bulk velocity	9.08 m/s
	U_{cross}	9.43 m/s
	Turbulence intensity	1.5%
	Re	$6.24 \cdot 10^{4}$
	Turbulence length scale	$7.56 \cdot 10^{-3}$
Jet inlet	Bulk velocity	37.72 m/s
	Turbulence intensity	7%
	Re	$1.92 \cdot 10^{4}$
	Turbulence length scale	$5.6 \cdot 10^{-4}$

In this study, passive scalar in STAR CCM+ was employed as the tracer for two-flow mixing to track scalar concentration in the fluid phase. The value of the dimensionless concentration was defined as 1 and 0 for jet nozzle inlet and crossflow inlet, respectively. For the crossflow outlet, pressure outlet boundary condition was chosen. The pressure was specified to reference pressure of 101325 Pa. The other surfaces were assigned as smooth walls with no-slip condition. However, when the half domain was applied for the simulation, the surface with the plane y=0 was defined as symmetry plane.

3.2.3 Computational mesh

In this study, the mesh details were collected from previously used mesh strategies in SGT-750 and SGT-800 projects at combustion team, Siemens Energy AB, Finspång where the grid in the gas turbine model could be simplified into three main meshing regions: upstream, jet refinement and downstream shown as red, yellow, and green, respectively in Figure 10. When details of the previously used mesh strategies were transferred to the simplified JIC case, cell size and refinement size were increased with a geometrical scaling factor based on the nozzle diameters. Since gas turbine fuel nozzles are typically of the order to 1 mm and the JIC jet diameter is 8 mm, the sizes were scaled up accordingly. Regarding to this, meshing in the actual gas turbine model could fit the simplified JIC configuration and the accuracy could be further evaluated.

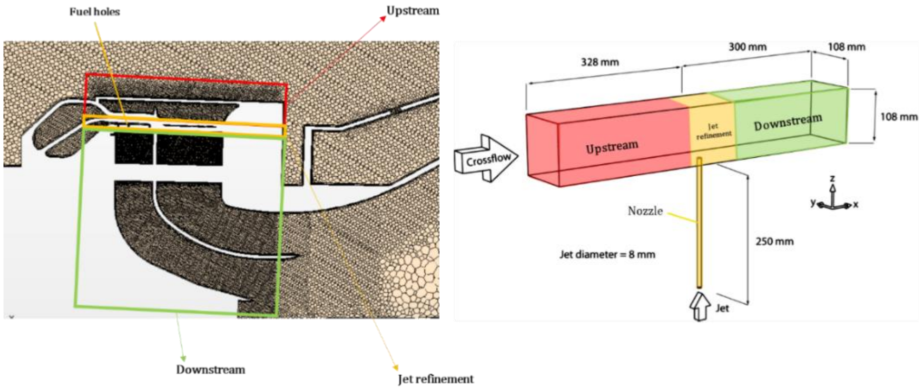

Figure 10. Meshing concept: Example from main 1 and main 2 channel of SGT-750.

In this study, four previously used mesh strategies were investigated. All the mesh scenes at symmetry plane are illustrated in Figure 11 and grid information of each mesh are represented in Table 2 and in Appendix B1. It can be noted that no refinement was included in C1 while C2, C3, and C4 composed of grid refinement bounded by different geometrical shapes either block, cylinder or sphere. Mesh C2 composed of two level upstream regions, also for downstream together with jet refinement region bounded by a large diameter cylinder. For mesh C3, a small sphere was attached to the nozzle outlet with a rectangular block to cover the important jet region. While mesh C4 included a cylinder extended down to jet nozzle and horizontal cylinder attached to the wall in the crossflow channel. In addition, a polyhedral mesh with 5 prism layers (0.0012 m total thickness) at the walls were applied for all previously used mesh strategies. The base size for all standard meshing cases was fixed to 8 mm. When grid sensitivity was performed the base size was further adjusted either larger or smaller than 8 mm depending on the targeted cell count.

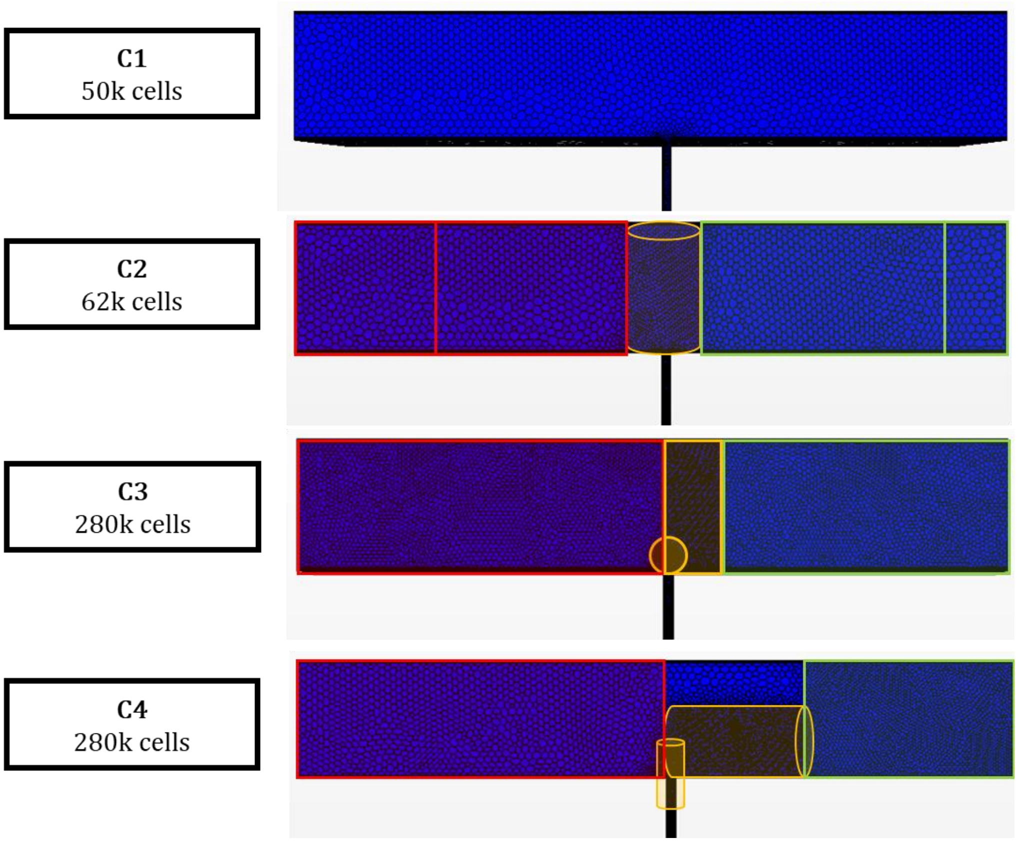

Figure 11. Mesh strategies based on previous gas turbine models visualized at symmetry plane y=0; Red denotes upstream, Yellow denotes jet refinement, Green denotes downstream.

Table 2. Detail of previously used mesh strategies.

		Previously used mesh strategy			
		C1	**C2**	**C3**	**C4**
Obtained from		SGT-750	SGT-750 LES	SGT-800	SGT-750 RANS
Cell count		50k	62k	280k	280k
Element size (mm) *adjusted to JIC	**Jet wall**	1	3.125	0.656	0.637
	Jet pipe	1	3.125	0.656	0.68
	Upstream	7.5	Upstream1: 31.25 Upstream2: 12.50	3.93	6.12
	Jet refinement	7.5	3.125	Jet1 (sphere): 0.656 Jet2(cylinder): 1.31	Jet1 (cylinder): 0.68 Jet2 (cylinder): 1.36
	Downstream	7.5	Downstream1: 6.25 Downstream2: 12.5	3.93	3.4
Mesh type		Polyhedral			
Prism layers		5			

3.2.4 Model formulation

The selected models for the study are shown in Table 3. Default values from STAR CCM+ were used for any parameters which are not shown in the table.

Table 3. Physics continuum models.

Parameters	**Enabled model**
Space	Three dimensional
Time	Steady (for realizable k-epsilon and lag EB) Implicit unsteady (for LES and SST k-omega)
Material	Air ($\rho = 1.185$ kg/m^3 and $\mu = 1.831$e-5 kg/ms)
Reacting regime	Non reacting
Viscous regime	Turbulent
Flow	Segregated flow
Enthalpy	Segregated fluid isothermal (298 K)
Equation of state	Ideal gas
Turbulence model	Realizable k-epsilon LES Lag EB k-epsilon SST k-omega
Gradient matrices	Gradient
Wall treatment	All y+ treatment
Subgrid scale turbulence (for LES)	WALE subgrid scale
Optional model	Passive scalar ($Sc_t = 0.9$)

For the JIC simulation, it was assumed isothermal condition and ideal gas equation of state. Air has been used for the whole simulation domain. Passive scalar model was applied as optional tracer model to track mixing behavior in terms of dimensionless scalar concentration. Turbulent Schmidt number (Sc_t) defined as the ratio between turbulent viscosity (υ_t) and turbulent diffusivity (Γ_t) was employed to describe turbulent mixing. The general approach used a value of 0.9 for typical cases.

For the flow solver, segregated flow algorithm was used due to its lower memory cost and faster rate of convergence compared to the coupled flow solver. In terms of time solver, steady state condition was applied for realizable k-epsilon and lag EB k-epsilon model, while implicit unsteady solver was chosen for transient simulation of LES and SST k-omega model. Note that the main reason for simulating SST in transient state originated from unconverged results when steady time solver was initially selected. More information of the transient simulation is presented in section 3.2.6. In order to achieve results with low numerical diffusion, second order upwind scheme of convection discretization was used for all turbulence models. In addition, all y+ treatment was chosen as near-wall region model for all cases. Overall mesh strategies provided approximate mean y+ of 3 with the lowest value of 1 and maximum value of 16.

3.2.5 Analysis of results

In this study, 4 important parameters including velocity component in x direction (U), dimensionless concentration of the passive scalar (C), mass flow center coordinate of the dimensionless concentration (C_m) and radial root mean square deviation (RMSD) were considered.

For the velocity component (U), several line probes were generated from x/D=1 to x/D=10 covering the important jet trajectory region at the symmetry plane y=0 as shown in Figure 12. Experimental data was available for this parameter from the study of Siemens Energy in collaboration with Karlsruhe Institute of Technology, Germany [1].

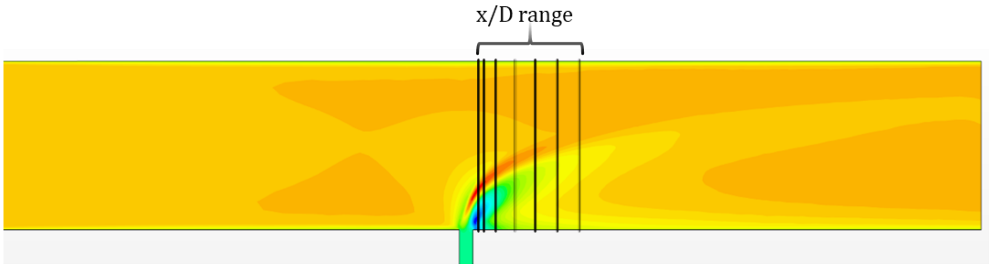

Figure 12. Line probes measuring velocity component in x direction at symmetry plane.

Another parameter where experimental data was available for validation was dimensionless concentration (C) at the symmetry plane. Three line probes including z/D=1.5, z/D=3, and z/D=4.5 were used to measure and visualize concentration as illustrated in Figure 13.

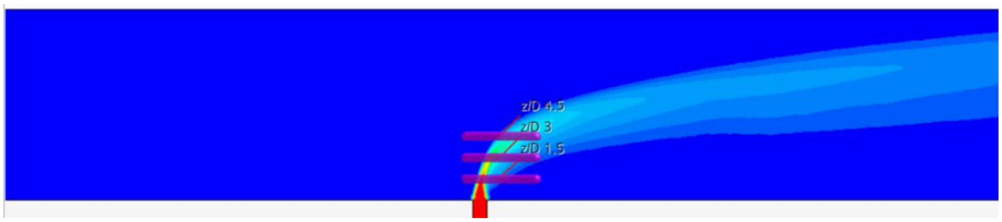

Figure 13. Line probes measuring dimensionless concentration at symmetry plane.

In addition, several cross section planes from x/D=0.5 towards the crossflow outlet were generated in STAR CCM+ as depicted in Figure 14. The mass flow center coordinate of the dimensionless concentration (C_m) was calculated using Equation (59) in each plane to determine the center location on the y and z plane by weighting according to the mass flow of concentration.

$$C_m = \frac{\sum\{(\rho \cdot v_{axial} \cdot A \cdot C) \cdot |x\_i|\}}{\sum(\rho \cdot v_{axial} \cdot A \cdot C)} \tag{59}$$

Where, v_{axial} =axial velocity (m/s)
A = cell area (m^2)
C = dimensionless concentration (passive scalar)
x_i = coordinate position (y, z)

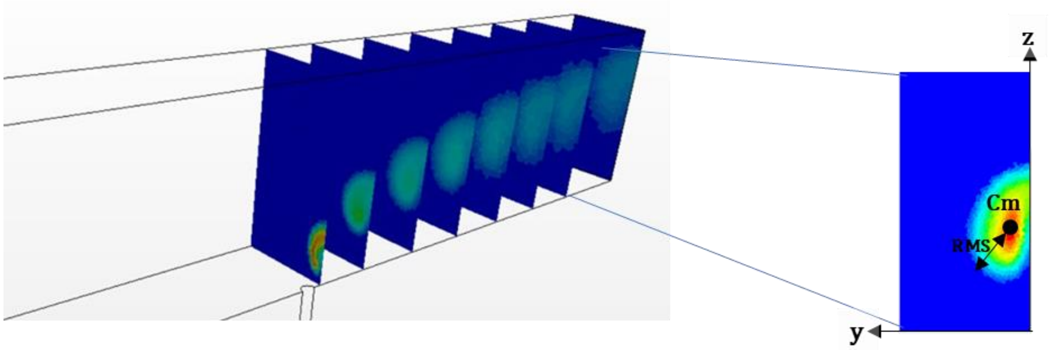

Figure 14. Plane sections of passive scalar showing mass flow coordinate of dimensionless concentration and radial root mean square.

Moreover, the radial root mean square deviation (RMSD) defined by Equation (60) was also calculated throughout each cross section plane in Figure 14 to investigate the spreadout of concentration in each plane towards downstream region.

$$RMSD = \sqrt{\frac{\sum\{\rho \cdot v_{axial} \cdot A \cdot C \cdot ((y - C_{my})^2 + (z - C_{mz})^2)\}}{\sum\{\rho \cdot v_{axial} \cdot A \cdot C\}}} \tag{60}$$

3.2.6 Transient simulation guidelines

The use of transient simulations, especially LES turbulence models has been increasing in the gas turbine industry due to its high accuracy compared to RANS turbulence models. However, it requires high computational cost, and therefore the simulation set up needs to be well adjusted to minimize the computation cost.

Initialization

For LES simulations in this study, realizable k-epsilon model with steady state condition was initially performed until residuals and all monitoring indicators were stabilized. The solution from steady simulation was used as initial condition for LES to get the correct mean field. The simulation was then switched to LES transient mode with WALE subgrid scale model.

Solvers and discretization

In order to ensure a good LES results, a suitable time step is required. The time step was determined by Convective Courant-Friedrichs-Lewy number (CFL). Its definition includes cell size (Δx), velocity scale (U) and time step size (Δt) as shown in Equation (61). Time step used in the simulation should be less than the time which flow properties transfer from one cell to the neighbor cell. Thus, CFL should be less than 1 for the important jet region.

$$CFL = \frac{U\Delta t}{\Delta x} \tag{61}$$

In this study, time step in LES simulation was adjusted to 6e-6 s according to the aim to achieve CFL number lower than 1 in the important jet region. The time step of 1e-5 s was applied for transient SST k-omega simulation since typical CFL for RANS simulation can be higher than LES (5-50) in order to save computational time. 15 inner iterations were used for all transient simulations and the second order temporal discretization was applied.

Data sampling

Field monitors of interest such as mean velocity, mean of passive scalar, field mean of pressure, field variance of velocity component, etc. were defined before starting the simulation. The starting time to collect the data samples were determined by the number of 'flow-through times', i.e. the time for a fluid particle to pass through the whole domain. According to the geometrical domain of JIC, crossflow planar channel has approximated 0.07 s of residence time, calculated from velocity and channel length. The simulations were run for 3-4 flow-through times before data averaging was initiated to eliminate the data sampling being affected by the initial conditions. This was confirmed from the fluctuation which was monitored in the point probes distribution as shown in Figure 15. Afterwards, the data sampling was initiated, and the simulations were further simulated for approximately 15 flow-through times until the mean values of interest became stable to ensure reliable statistics.

LES assessment

According to the literature [16], at least 80% of turbulent kinetic energy should be resolved in LES. This corresponds to the ratio of resolved turbulent kinetic energy (k_r) to the overall turbulent kinetic energy ($k_r + k_{SGS}$) as shown in Equation (62).

$$\frac{k_r}{k_r + k_{SGS}} > 0.8 \tag{62}$$

Here, k_r and k_{SGS} was calculated from Equation (63) and Equation (64), respectively. Note that the RMS values were obtained from the square root of field variance data.

$$k_r = \frac{1}{2}({v_{x,RMS}}^2 + {v_{y,RMS}}^2 + {v_{z,RMS}}^2) \tag{63}$$

$$k_{SGS} = \frac{C_t \mu_t \mathbf{S}}{\rho} \; ; \; C_t = 3.5 \tag{64}$$

In addition to the subgrid viscosity ratio, the ratio of turbulent viscosity (μ_t) to laminar viscosity (μ) was also used to measure the effect of unresolved scales to the LES results. The smaller value of subgrid viscosity ratio the more preferable.

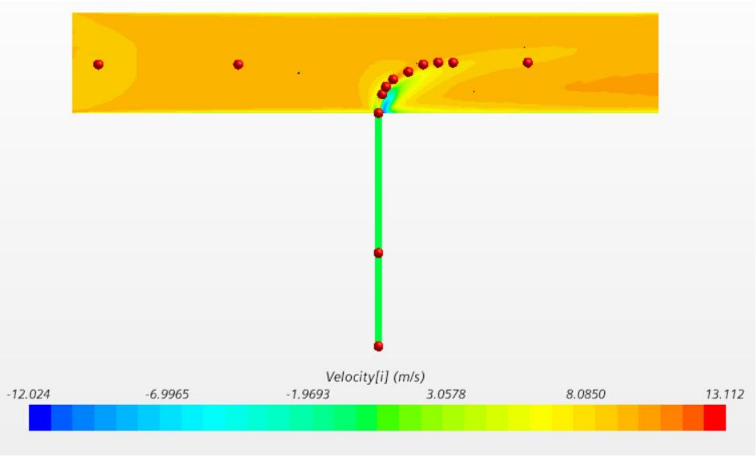

Figure 15. Point probes for LES simulation.

3.3 Adaptive meshing

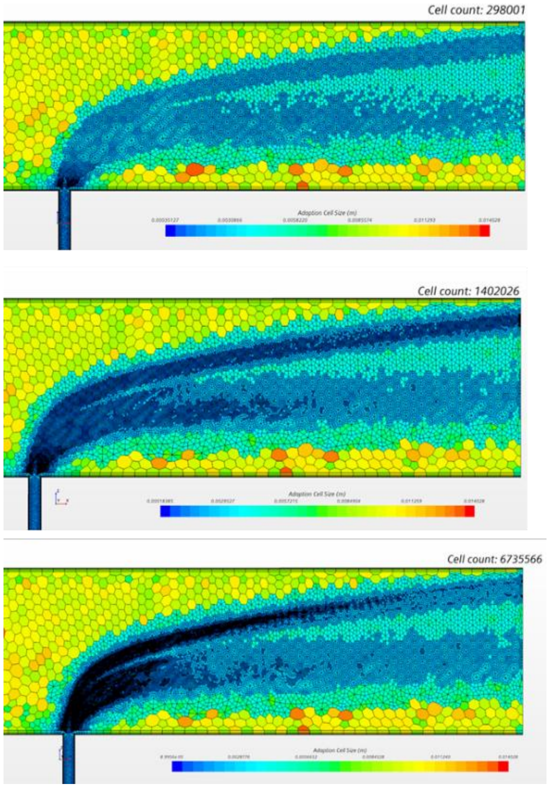

Figure 16. Contour plot of adaption cell size; refinement level 2 (top), refinement level 3 (middle), refinement level 4 (bottom).

One objective of this study is to verify grid independence for both previously used mesh and optimized mesh strategies. For a proper mesh independency test, typically the cell size should be reduced to half in all directions which means about 8 times more cells, thus, high cell count is needed. An alternative approach to perform the mesh independence test is to use Adaptive Mesh Refinement (AMR) in STAR CCM+. In this study, the mesh C1 without any refinement was used as the base mesh. The mesh was refined based on the local concentration gradient in the range of 0.01 to 1.15. The transition width which specifies the cell width of the translational layer between different refinement levels was fixed to stable value of two. Refinement level indicates the number of cell subdivision. The higher refinement level, the more cell count is obtained. In this study, refinement level was varied from two to four. The cell count was increased from 300k cells to 7M as shown in Figure 16.

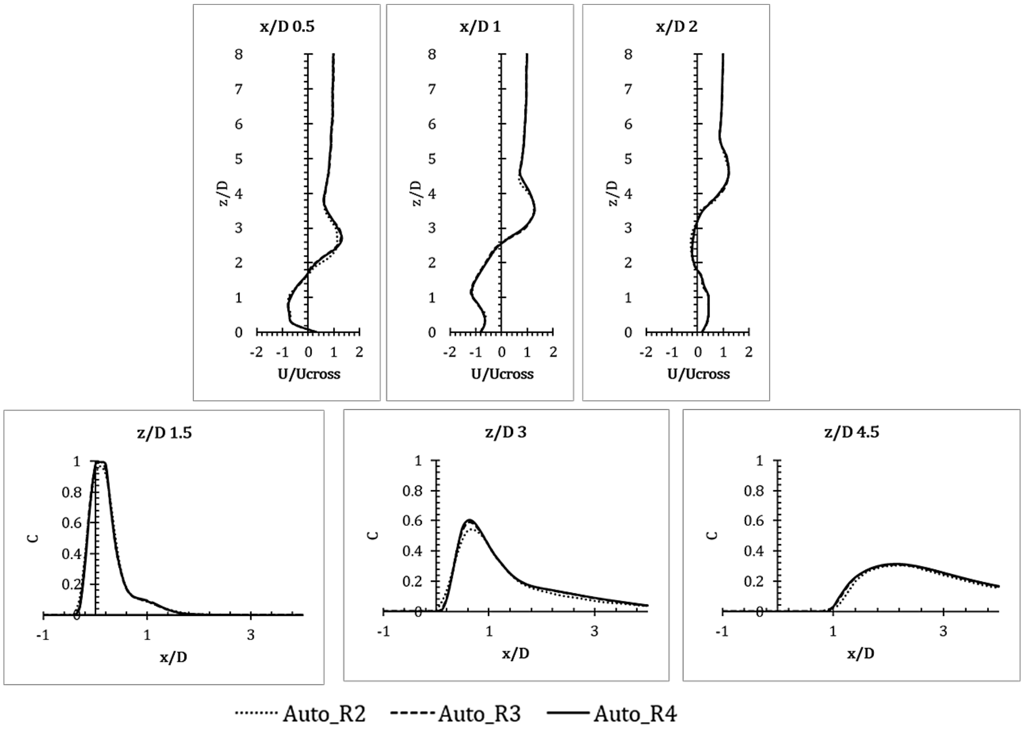

Figure 17. Velocity component and dimensionless concentration plots at symmetry plane for mesh independence test

Figure 17 illustrates that the deviation of both mean velocity and concentration was very small. Thus, adaptive mesh could be used as grid independence confirmation as a high cell count sensitivity mesh.

3.4 Previously used mesh strategies

To investigate the performance and accuracy of the previously used mesh strategies shown in Figure 11, realizable k-epsilon and LES turbulence models were applied to the simulation in order to observe JIC in steady state and transient state environments, respectively.

3.4.1 Previously used mesh strategies and realizable k-epsilon

Firstly, steady state realizable k-epsilon simulation was performed on four previously used mesh strategies. Figure 18 shows x-velocity component on x/D=0.5 to x/D=4 and dimensionless concentration on z/D=1.5 to z/D=4.5 at the symmetry plane. Velocity appeared to be more sensitive to the mesh in the upstream region while velocity downstream was not affected much by the grid, thus velocity component on further downstream locations were not included. However, effect of the mesh resulted in high sensitivity of dimensionless concentration for all observed regions.

From Figure 18, it can be observed that mesh C1 and C2 were not able to predict velocity component and concentration well since the results highly deviate from the experimental data. In contrast, C3 and C4 resulted in good agreement with experimental data for both velocity and concentration. This can be explained by rules of thumbs for jet resolution. In order to resolve the fuel jet and the jet penetration into the crossflow, sufficient mesh resolution is needed. This can be ensured by the use of a couple of rules of thumbs. To obtain good jet resolution, the mesh should possess these criteria.

1. The mesh should have at least 10 cells over the hole diameter. Since the diameter of jet nozzle in this study was fixed to 8 mm, the cell size should be less than 0.8 mm.
2. The mesh should contain minimum 30 cells over the circumference which means that cell size should be less than 0.84 mm according to this criterion.

Details of the element size shown in Table 2 revealed that C1 and C2 needed improvement of the cell size distribution.

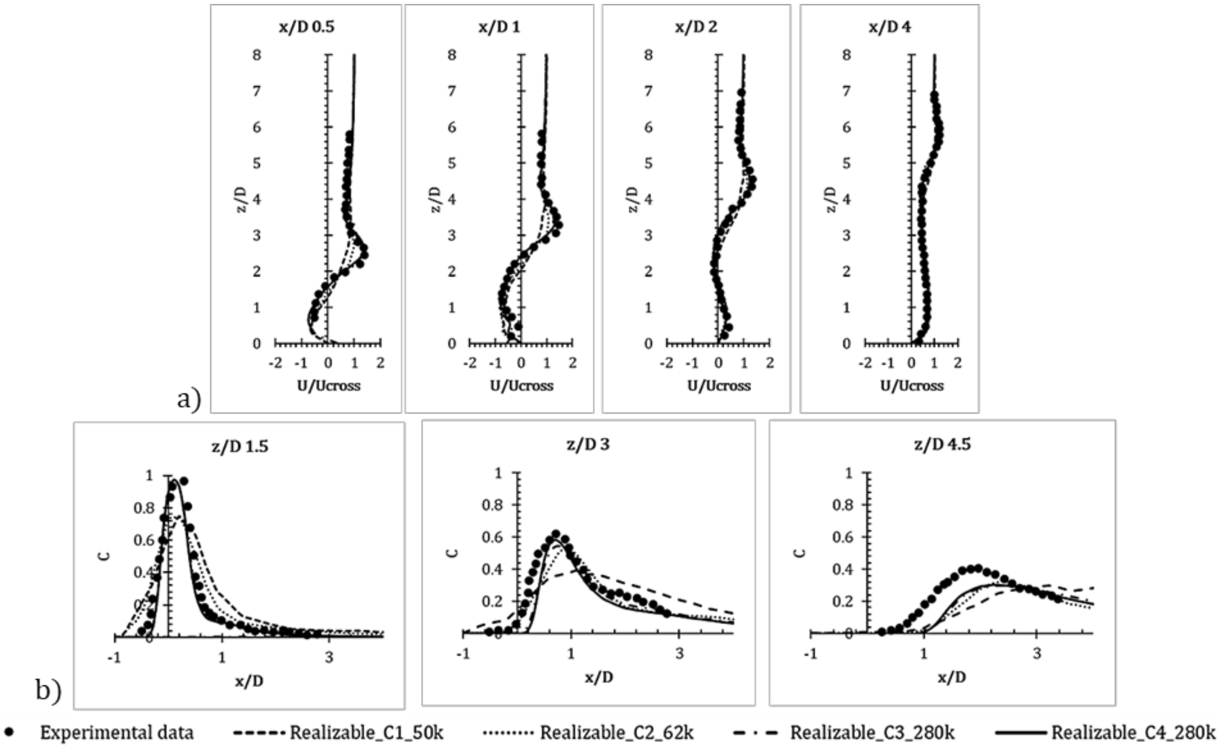

Figure 18. Results of previously used mesh strategies with realizable k-epsilon model: (a) Velocity component at symmetry plane y=0. (b) Dimensionless concentration at symmetry plane y=0.

To provide a better illustration of the accuracy of the previously used mesh strategies, contour plots of the dimensionless concentration at z/D=1.5 are presented in Figure 19. It is revealed that mesh C1 and C2 result in a large difference compared to experimental data. Concentration in the middle region obtained from mesh C1 and C2 were much lower than the actual concentration. Thus, mesh C3 and C4 were selected for the further study of grid sensitivity test.

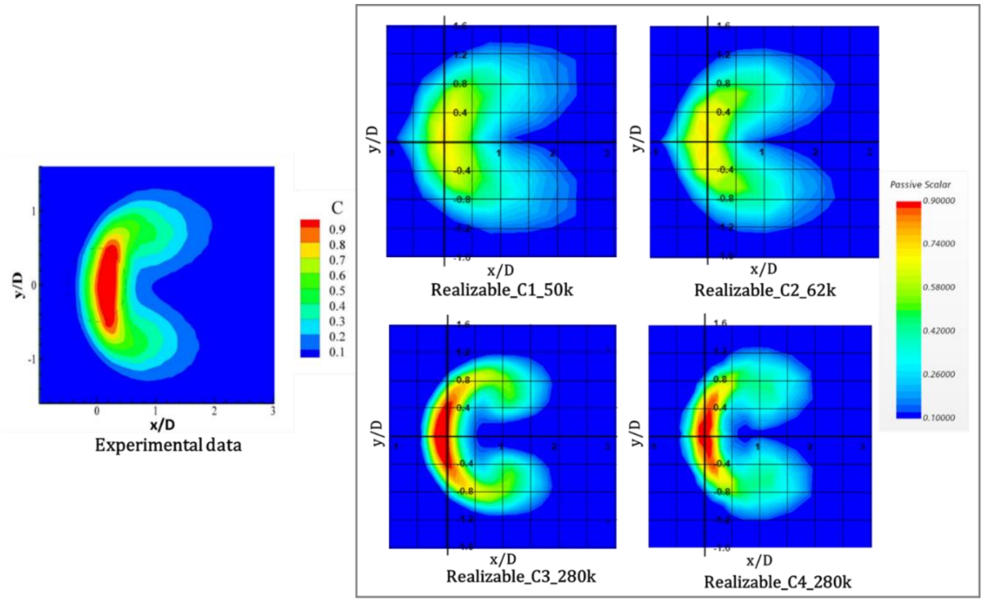

Figure 19. Results of previously used mesh strategies with realizable k-epsilon model: Two dimensional maps of dimensionless concentration at z/D=1.5.

3.4.2 Previously used mesh strategies and LES

By comparing the velocity distribution with the results using realizable k-epsilon, Figure 20 illustrates that reliability of mesh C1 did not improve when using LES model and moreover, mesh C3 and C4 overpredicted the velocity component in the peak regions. By observing the concentration in Figure 20, it can be clearly seen that mesh C1 and C2 required more grid improvement in order to resolve the concentration field correctly. Regarding to the results from both realizable k-epsilon and LES turbulence models, the grid sensitivity test was performed only for mesh C3 and C4.

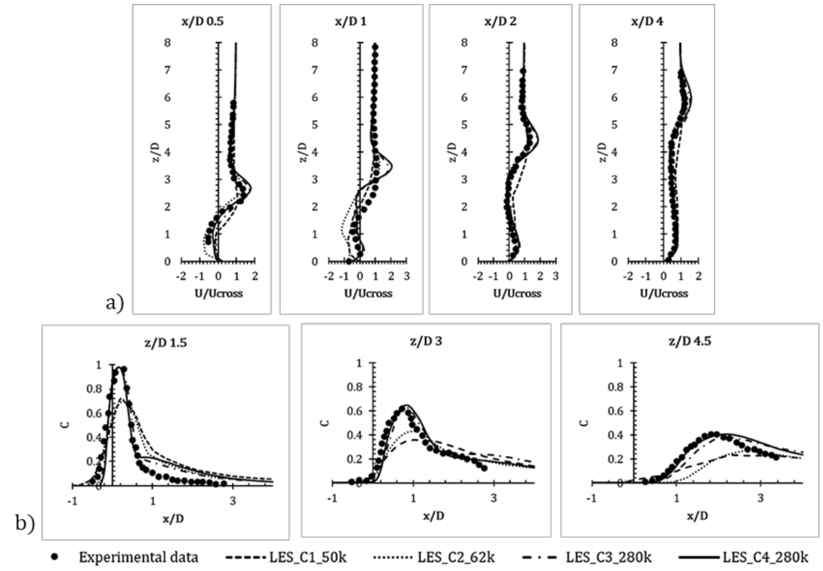

Figure 20. Results of previously used mesh strategies with LES model: (a) Velocity component at symmetry plane y=0. (b) Dimensionless concentration at symmetry plane y=0.

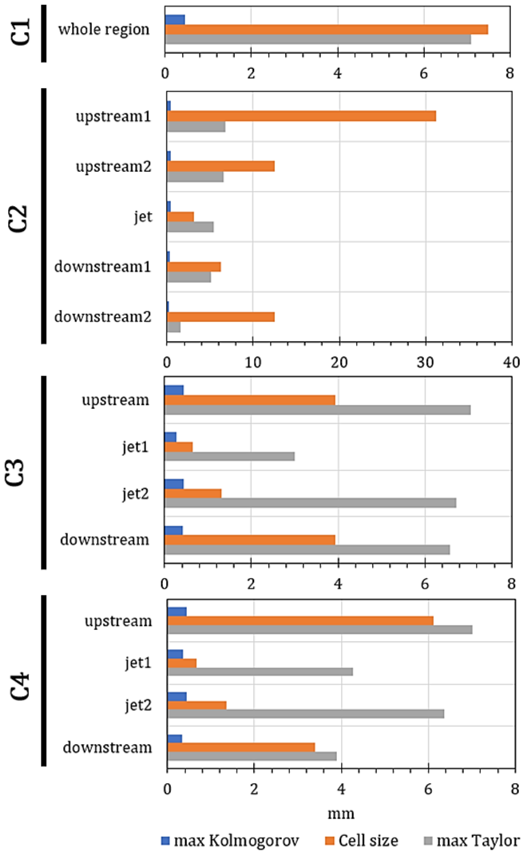

Figure 21. Kolmogorov scale, Taylor microscale and cell size of each part of previously used mesh strategies.

In order to assure that all large eddies can be resolved, and small eddies can be modelled below inertial subrange, computational cell size needs to be investigated according to LES guidelines [16]. The reasonable cell size (Δ) to be applied in LES simulation should be in the range $\eta<\Delta<\lambda$ where Kolmogorov length scale (η) is the indication of the local minimum cell size of eddies and Taylor microscale (λ) is the denotation of the local maximum size of eddies in inertial subrange.

According to Figure 21, the computational grid size of mesh C1 were slightly out of the range. The actual cell size was higher than the maximum Taylor microscale. This may lead to the bad agreement of the results comparing to the experimental data. Same circumstance occurred for the whole domain of mesh C2 except in jet refinement region, thus, the results obtained from mesh C2 were not good enough. For mesh C3 and C4, the cell sizes were suitable for LES simulation for the whole domain.

Additionally, energy resolution can be evaluated by the ratio of resolved energy amount (k_r) to overall turbulent kinetic energy ($k_r + k_{sgs}$). According to the best practice guidelines, more than 80% of energy must be resolved for reasonable resolution in LES. From Figure 22, about 90% of energy could be resolved for large part of the important region of jet trajectory for mesh C2, C3 and C4, even though some local regions did not fulfill this. Mesh C1 was far from fulfilling this. However, the region of jet nozzle and crossflow inlet were under-resolved for all cases except mesh C3 and C4 where the turbulent kinetic energy was solved to some extent upstream.

The subgrid viscosity ratio can be used to measure importance of unresolved scale. The smaller viscosity ratio the better LES resolution. According to Figure 22, turbulent viscosity ratio was significantly lower throughout the region for mesh C2, C3 and especially, mesh C4 as compared to mesh C1. Thus, mesh C4 occurred to be the best mesh in this case, even though it is not clear what level of subgrid ratio that may indicate sufficiently resolved mesh distribution.

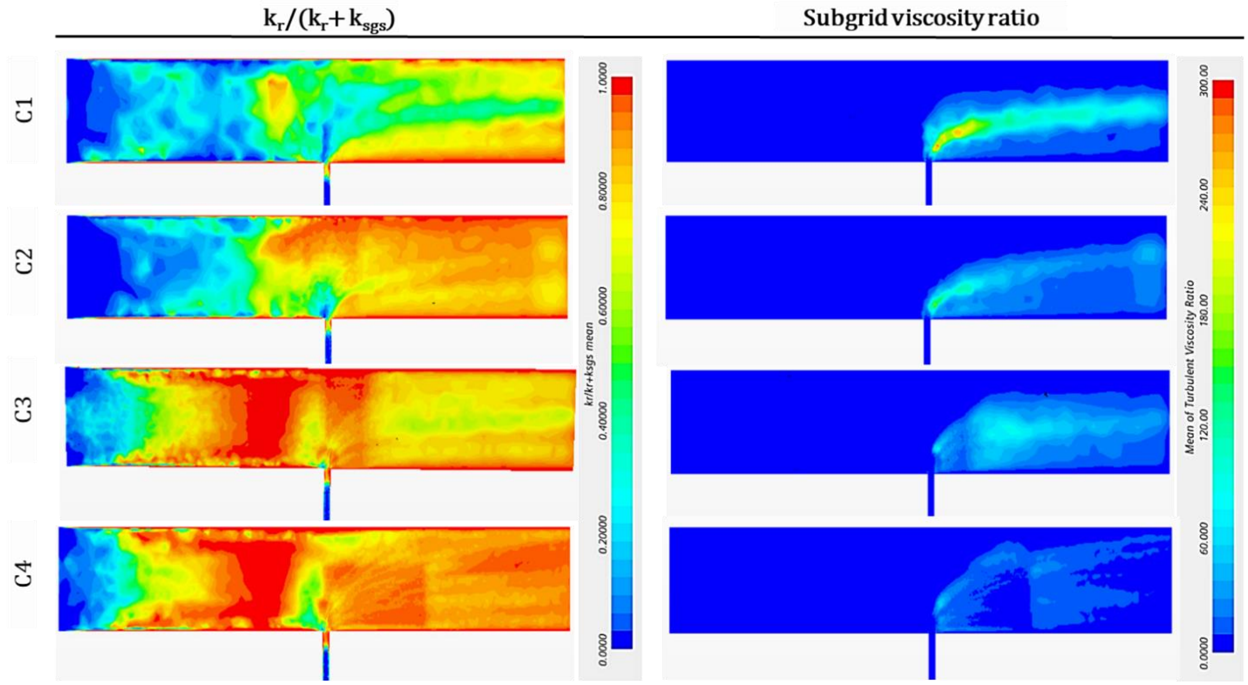

Figure 22. Results of previously used mesh strategies with LES model: (Left) Contour plot of resolved turbulent kinetic energy ratio at symmetry plane. (Right) Contour plots of subgrid viscosity ratio at symmetry plane.

3.4.3 Grid sensitivity test

Grid sensitivity test was performed on mesh C3 and C4 by adjusting the base size to lower the cell count down to 50k cells. The finest mesh was achieved using Adaptive Mesh Refinement (AMR) to confirm grid dependency. The purpose of grid sensitivity test was to observe the differences of mesh C1, C2, C3 and C4 when the same cell count was applied.

Since the mesh strategy of C2 did not allow good prediction of the interested parameters, C3 and C4 strategies could be applied due to their good agreement with experimental data for all parameters when applying both RANS and LES turbulence models. However, that would affect the computational cost and especially for combustion systems with many fuel nozzles. SGT-750 using 8 combustors and SGT-800 using 30 burners in an annular combustor have similar total amount of fuel nozzles, but a one burner sector CFD model of SGT-750 would have about 30/8 more fuel nozzles than SGT-800. Therefore, it is more important to keep the mesh resolution down for SGT-750 where the mesh strategies of C3 and C4 would require about 20M additional cells compared to C2. Thus, the aim of grid sensitivity test was to achieve high accuracy for both velocity component and concentration when the cell count of mesh C3 and C4 were lowered down from 280k to mesh C2 cell count, 62k cells.

Similar results of velocity component and concentration from grid independence test of C3 and C4 were obtained (Appendix B2). However, in order to determine the differences between C3 and C4, the mass flow center dimensionless concentration (C_m) and radial root mean square deviation (RMSD) were used in order to quantify the spread-out of concentration on each plane. These two parameters are illustrated in Figure 23 in the log scale on x axis. It is observed from all plots that from 300k cell of adaptive refinement mesh, small grid dependency occurred where 280k cells of mesh C4 showed the result most similar to the adaptive mesh. When comparing with mesh C3, the result of mass flow center location started to deviate from the adaptive mesh study at x/D=20 which is considered to be worse than mesh C4. All parameters related to concentration revealed that lowering the cell count of mesh C3 and C4 under 280k cells was not reliable enough due to large grid dependence. However, mesh C4 occurred to be the most promising mesh strategy for further improvement with the goal to increase grid independency when the cell count was lowered down to 62k.

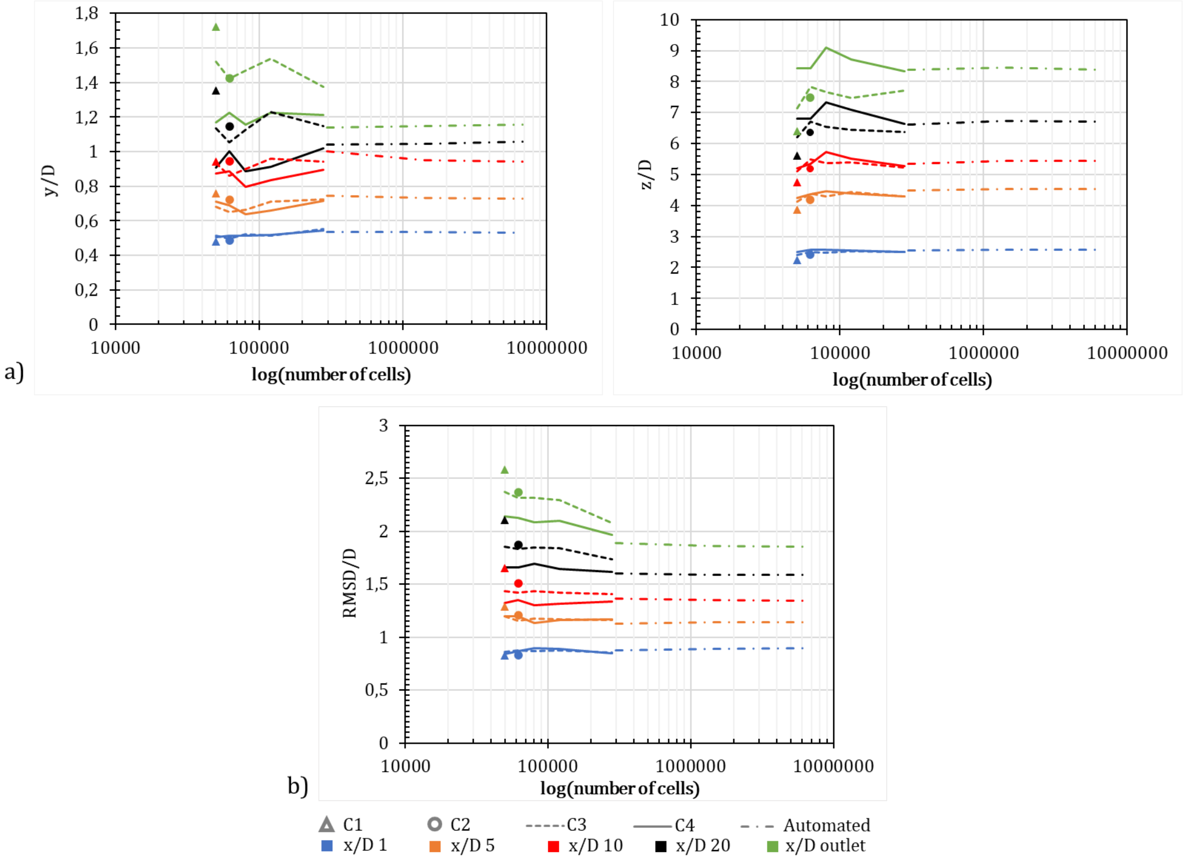

Figure 23 Results of mesh strategies C3 and C4: (a) Mass flow center coordinate of the dimensionless concentration on different x/D planes (b) Radial root mean square deviation of mass flow concentration on different x/D planes.

4. Results and discussions

Mesh optimization approach is presented with an investigation of grid independency in this chapter. The results cover important parameters described in section 3.2.5. Moreover, the effect of turbulence models on the optimized mesh is also presented. Lastly, additional case studies using the optimized mesh strategy are shown.

4.1 Mesh optimization approach

The original C4 mesh strategy was further improved with the aim to achieve mesh independency by integrating adaptive mesh refinement. By using this approach to obtain the optimized static mesh, computational cost will be potentially lower compared to pure adaptive mesh refinement when the mesh model is applied with Design Manager to optimize the fuel holes location. Initially, section planes were generated on the adaptive mesh based on the magnitude of the concentration gradient and adaption cell sizes as depicted in Figure 24. Four planes were placed according to starting and ending locations of the proposed refinement regions. Important regions represented by small adaption cell size were investigated according to Figure 25 in order to obtain dimensions for geometrical shape part of volumetric refinement which could cover all high-magnitude concentration gradients. It is observed that the radius of high-magnitude gradient was larger towards downstream.

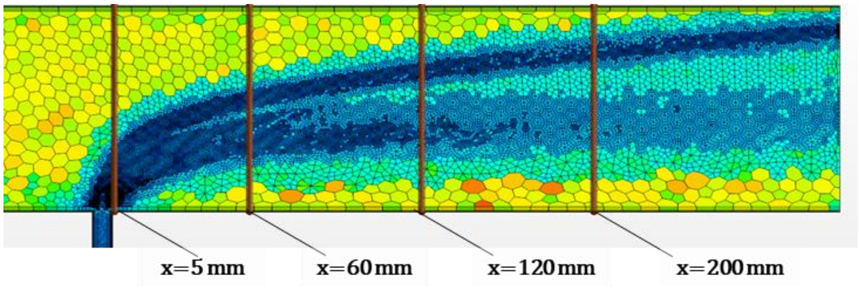

Figure 24. Section planes on adaptive mesh of 3rd level refinement.

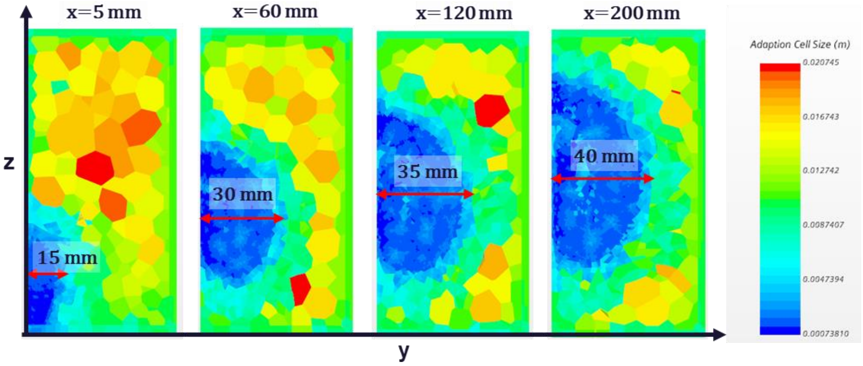

Figure 25. Contour plots representing adaption cell size on each section planes based on Figure 33.

Mesh C4 was modified by retaining the geometrical coordinates and cell sizes for both the upstream and downstream regions and altering only the jet refinement region. A cylinder and two-level cone were introduced. Their geometrical coordinates were adjusted according to radius obtained from Figure 25. Thereby, the first proposed mesh optimization strategy as shown in Figure 26 could cover all the region with large concentration gradient. The location and cell size of each refinement parts are shown in Table 4.

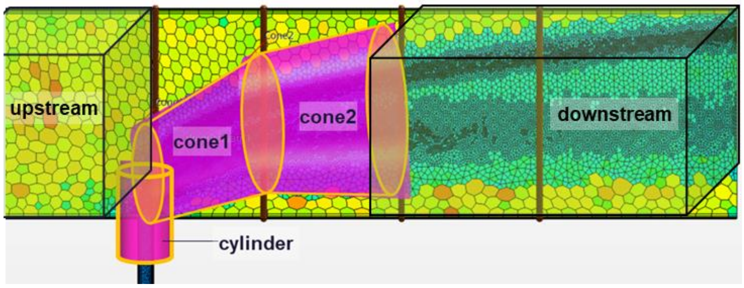

Figure 26. The first proposed mesh optimization strategy.

Table 4. Geometrical and cell size details of shape parts for the first proposed mesh optimization strategy (Strategy1).

	Start coordinate (mm)	End coordinate (mm)	Radius (mm)	Avg. cell size (mm)
upstream	[-328.0, 0.0, 0.0]	[-75.0, 54.0, 108.0]	-	6.12 (fixed)
cylinder	[0.0, 0.0, -20.0]	[0.0, 0.0, 35.0]	12	0.63
cone1	[5.0, 0.0, 25.0]	[70.0, 0.0, 50.0]	25,35	1.4
cone2	[55.0, 0.0, 48.0]	[130.0, 0.0, 55.0]	35,45	2.5
downstream	[125.0, 0.0, 0.0]	[300.0, 54.0, 108.0]	-	3.4 (fixed)

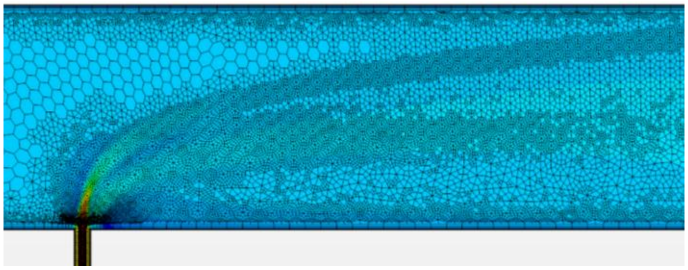

Figure 27 Adaptive mesh scene according to velocity and concentration gradient.

In addition to the initial mesh optimization strategy, three additional strategies as depicted in Figure 28 were also included in the study. According to the adaptive mesh refinement using both concentration and velocity gradient as refinement criteria, the mesh was highly refined at the wall as illustrated in Figure 27. Also, mesh sensitivity of velocity in the near-nozzle region was higher than the region downstream as mentioned in section 3.4*.* Thus, two more general strategies were investigated for the purpose of more generic cases and better refinement near the wall. The cones for jet refinement for strategy3 and strategy4 were attached to the wall. 1-level cone was included in strategy3 while 2-level cone was associated in strategy4. The details of geometrical shape part of strategy3 and strategy4 are depicted in Table 5.

4.1.1 Optimized mesh and realizable k-epsilon model

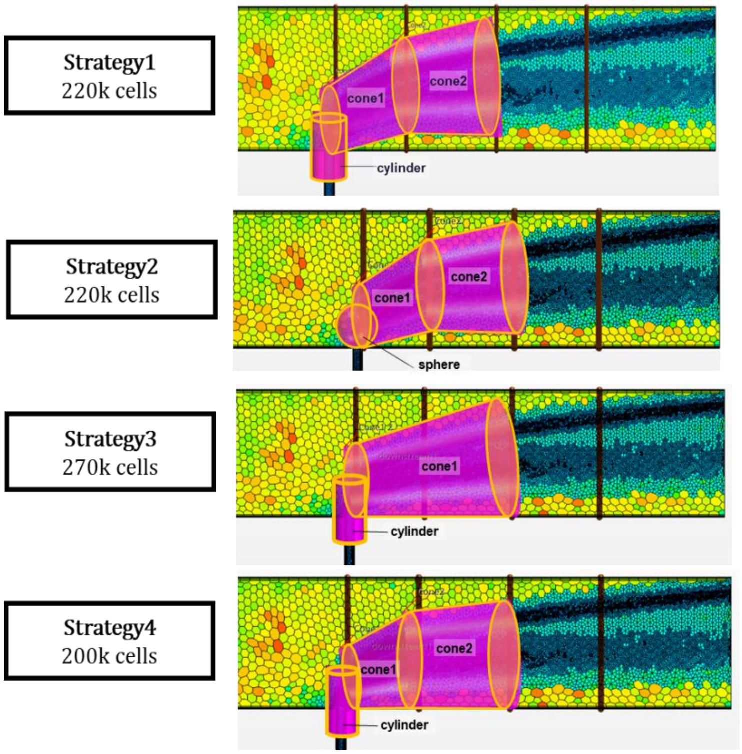

Figure 28. Mesh optimization strategies at symmetry plane y=0.

Grid independence test of the four mesh optimization strategies was performed by initially using realizable k-epsilon turbulence model. strategy1 with cylinder and strategy2 with sphere in jet refinement region depicted in Figure 28 revealed similar results of velocity and concentration and the variation against experimental data was in good agreement. The choice of either cylinder or sphere revealed small effects as illustrated in Figure 29. However, using a cylinder for the jet refinement region is more applicable since the length can be elongated and adjusted if the jet velocity would be increased. Thus, cylinder was chosen for the other strategies.

Table 5. Geometrical and cell size details of shape parts for strategy3 and strategy4.

Mesh strategy	Shape part	Start coordinate (mm)	End coordinate (mm)	Radius (mm)	Avg. cell size (mm)
strategy3	**cylinder**	[0.0, 0.0, -20.0]	[0.0, 0.0, 35.0]	12	0.63
	cone1	[5.0, 0.0, 30.0]	[125.0, 0.0, 50.0]	30,50	1.4
strategy4	**cylinder**	[0.0, 0.0, -20.0]	[0.0, 0.0, 35.0]	12	0.63
	cone1	[5.0, 0.0, 20.0]	[60.0, 0.0, 40.0]	20,40	1.4
	cone2	[45.0, 0.0, 40.0]	[130.0, 0.0, 45.0]	40,45	3.5 (fixed)

Figure 30 shows that strategy4 revealed higher grid independency than strategy3 and even better than mesh C4. This can be concluded from mass flow center coordinate on z axis where a straight line was obtained until x/D=20 for which the cell count could be reduced to 62k cells. Thus, strategy4 occurred to be the best mesh strategy obtained from this approach and strategy4 was used in the further study afterwards.

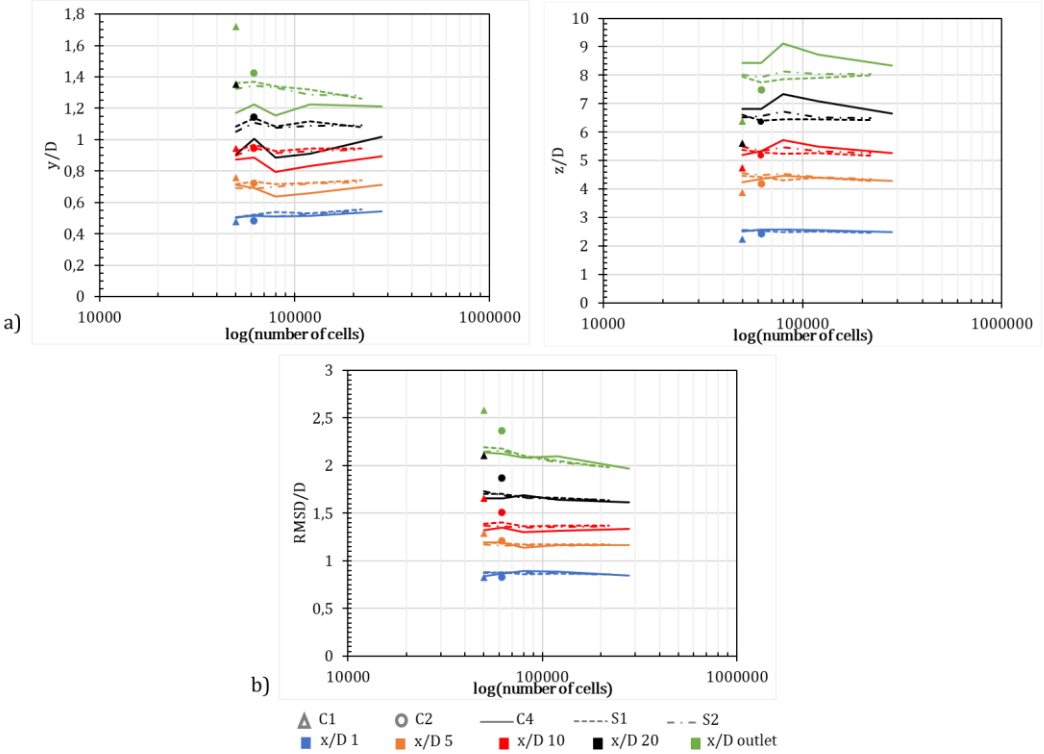

Figure 29. Results of strategy1 and strategy2 compared with mesh C4: (a) Mass flow center coordinate on different x/D planes . (b) Radial root mean square deviation of mass flow concentration on different x/D planes .

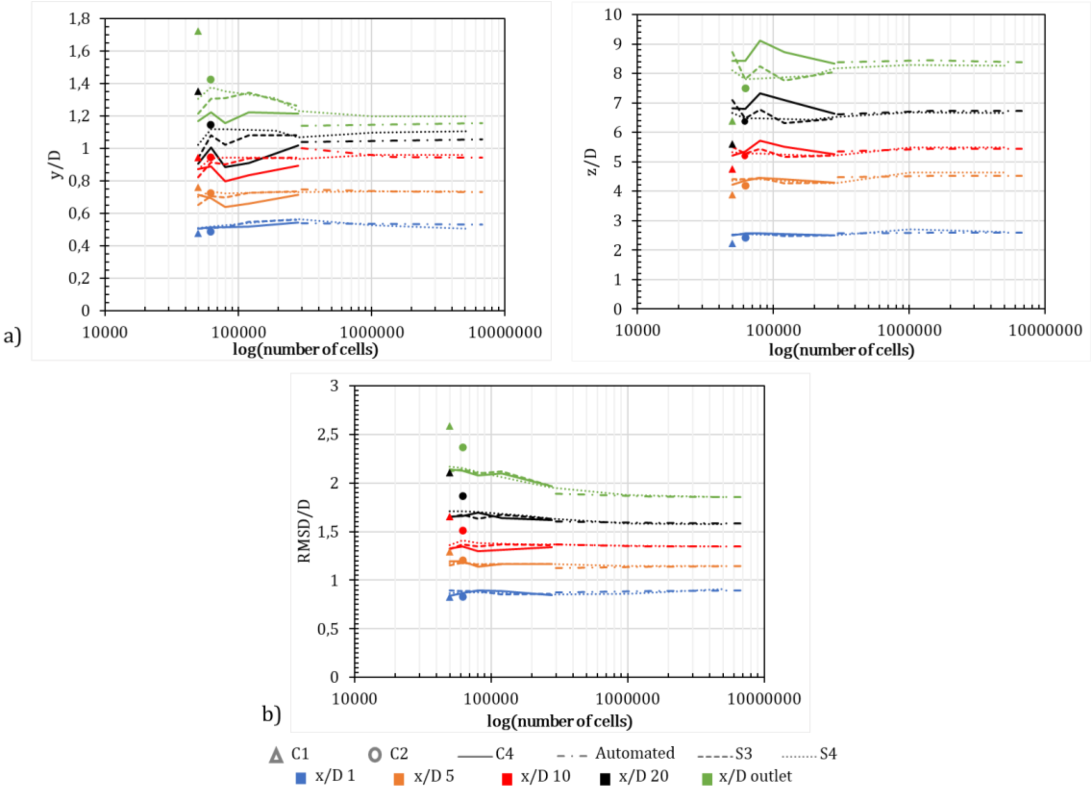

Figure 30. Results of strategy3 and strategy4 compared with mesh C4: (a) Mass flow center coordinate on different x/D planes . (b) Radial root mean square deviation of mass flow concentration on different x/D planes .

4.1.2 Optimized mesh and LES model

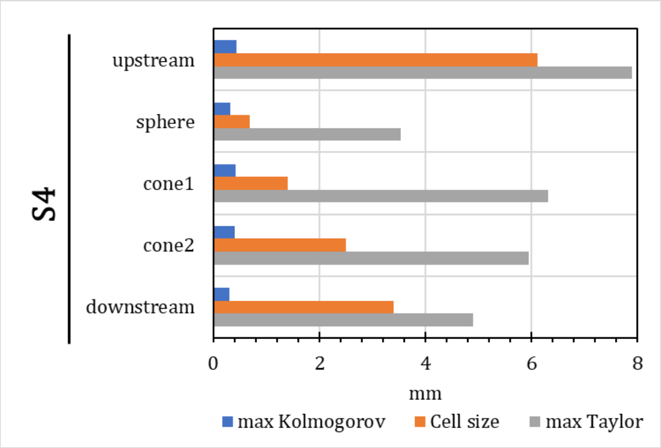

Figure 31. Kolmogorov scale, Taylor microscale and element size of each part of strategy4.

In order to investigate the efficiency and confirm grid independency of the optimized mesh, strategy4 was applied using the LES turbulence model where the full computational domain of JIC was applied. According to the Kolmogorov and Taylor microscale obtained from strategy4 in Figure 31, all cell sizes were in appropriate range in between Kolmogorov and Taylor scale. Thus, strategy4 was considered to allow good resolution of JIC in LES simulation.

Grid independence test was performed on strategy4 by varying the cell count from 62k to 2M. Figure 32 shows small variation of velocity component between the coarsest and finest mesh and the results agreed well with experimental data except some regions at the peaks. For concentration, strategy4 could accurately predict the concentration at peak in contrast to the realizable k-epsilon model. However, small variations are noticeable between the coarsest and the finest mesh.

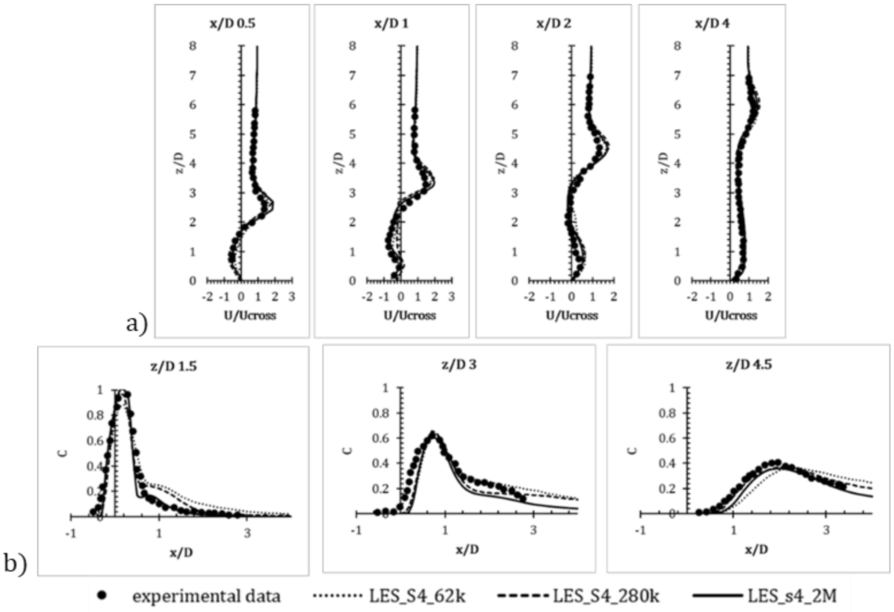

Figure 32. Results of strategy4 with LES model: (a) Velocity component at symmetry plane y=0, (b)Dimensionless concentration at symmetry plane y=0.

The energy resolution of strategy4 (280k cells) was investigated using the ratio of resolved turbulent energy (k_r) to overall turbulent kinetic energy ($k_r + k_{sgs}$) and subgrid viscosity ratio. Figure 33 illustrates that about 90% of the turbulent kinetic energy could be resolved for the important region from nozzle outlet to downstream. However, the jet nozzle region and crossflow inlet were under-resolved. In addition, turbulent viscosity ratio was considered low throughout the region indicating that unresolved scale was not important to the flow solution. Thus, strategy4 fulfilled requirement of LES simulation [16].

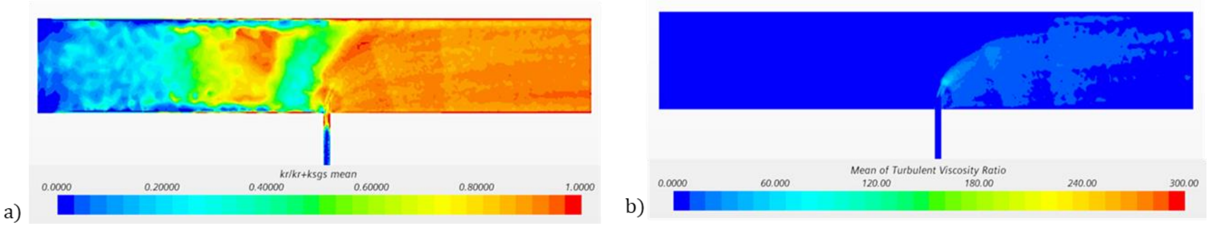

Figure 33. Results of strategy4 with LES model: (a) Contour plot of resolved turbulent kinetic energy ratio at symmetry plane, (b) Contour plots of subgrid viscosity ratio at symmetry plane.

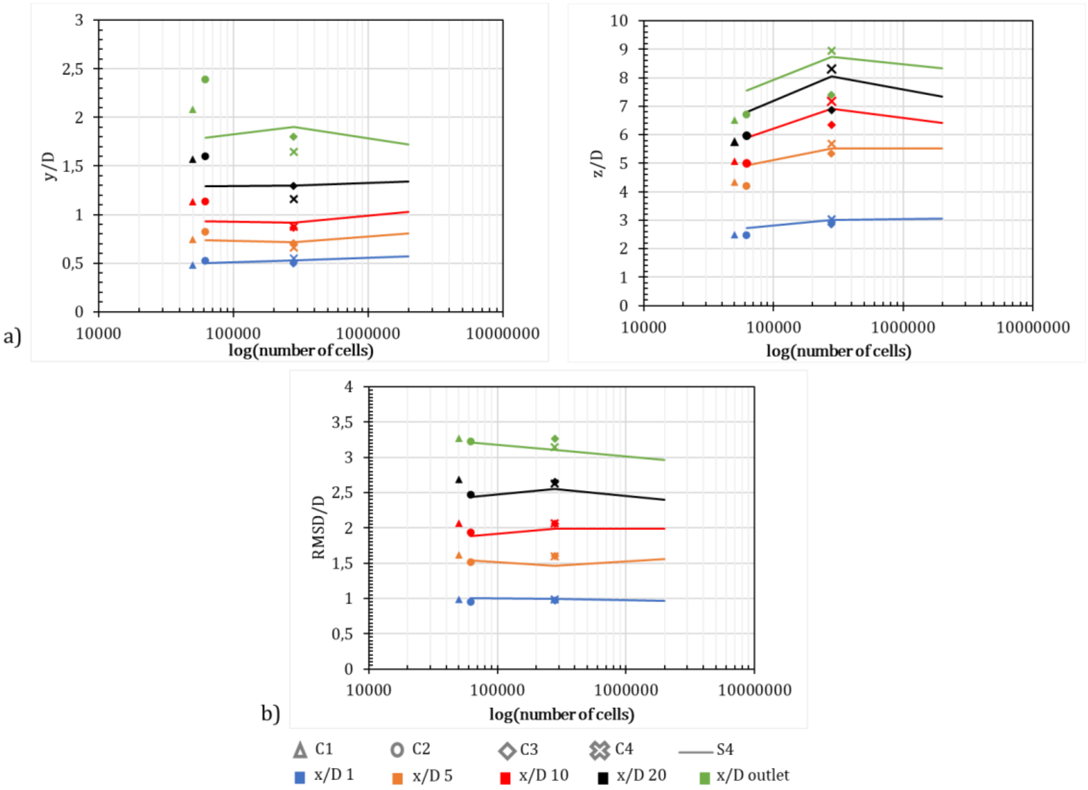

Figure 34. Comparison of previously used meshes and strategy4 for LES simulation
(a) Mass flow center of concentration on different x/D planes.
(b) Radial root mean square deviation of mass flow concentration on different x/D planes.

All LES results of concentration including previously used mesh strategies and strategy4 are presented in Figure 34. strategy4 showed small variation due to grid size with respect to mass flow center on y axis and z axis up to x/D=20 and x/D=5, and up to x/D=20 for the RMSD. When comparing strategy4 to mesh C3 and C4, the deviation is generally small. However, experimental data for mass flow center and RMSD of dimensionless concentration are required to further investigate the accuracy.

4.1.3 Turbulence model dependence

Four different turbulence models including realizable k-epsilon, LES, lag EB k-epsilon and SST k-omega were selected for the model sensitivity test of strategy4 where the cell count was fixed to 2M cells. Additionally, grid sensitivity test for each turbulence models can be found in Appendix C.

Considering the two main parameters, velocity component and dimensionless concentration for which experimental data was available, Figure 35 depicts high model dependency as large deviation occurred between different turbulence models. Thus, the turbulence model was regarded as one of the important aspects to investigate in order to achieve reliable solution of the flow. It can be concluded that the lag EB k-epsilon model was not the best model to predict velocity component and concentration for JIC. This was due to the large deviation of both velocity component and concentration compared to experimental data. The LES model slightly overpredicted the velocity in some peak regions but apart from that the agreement with measurement data is quite good. When considering concentration, SST k-omega was not able to accurately predict the passive scalar. It can be observed from z/D≥3 that SST k-omega model overpredicted the concentration peak. All in all, realizable k-epsilon and LES were found to be best suited for JIC simulation.

Regarding the mass flow center shown in Figure 36, strategy4 showed high grid independence when realizable k-epsilon, lag EB k-epsilon and LES were applied. In contrast, the SST k-omega model did not show grid independence compared to other models. Based on the radial root mean square, all turbulence models except the SST k-omega model showed low grid dependency in the region near the nozzle outlet and the deviation gradually increased towards the downstream region. However, strategy4 showed possibility to lower the cell count down to 62k throughout entire domain for realizable and lag EB turbulence models.

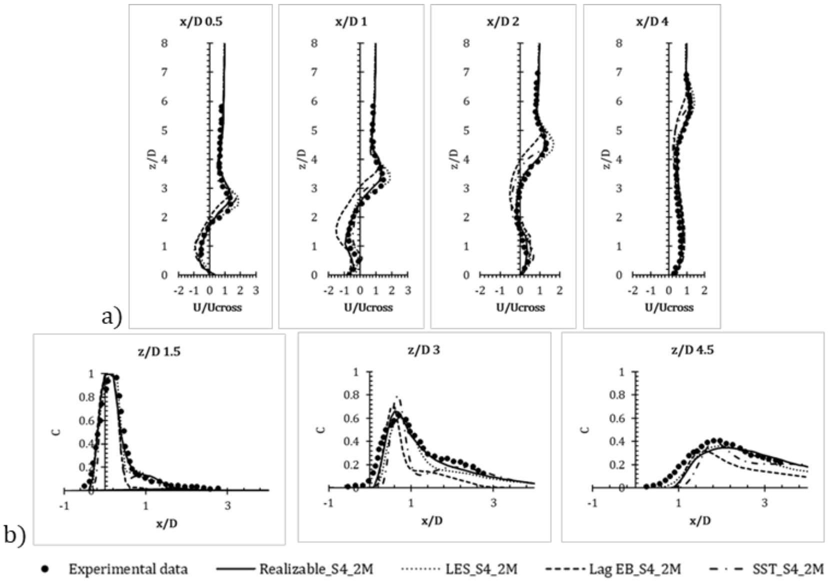

Figure 35. Results of strategy4 with various model including realizable k-epsilon, LES, lag EB and SST: (a) Velocity component at symmetry plane y=0. (b)Dimensionless concentration at symmetry plane y=0.

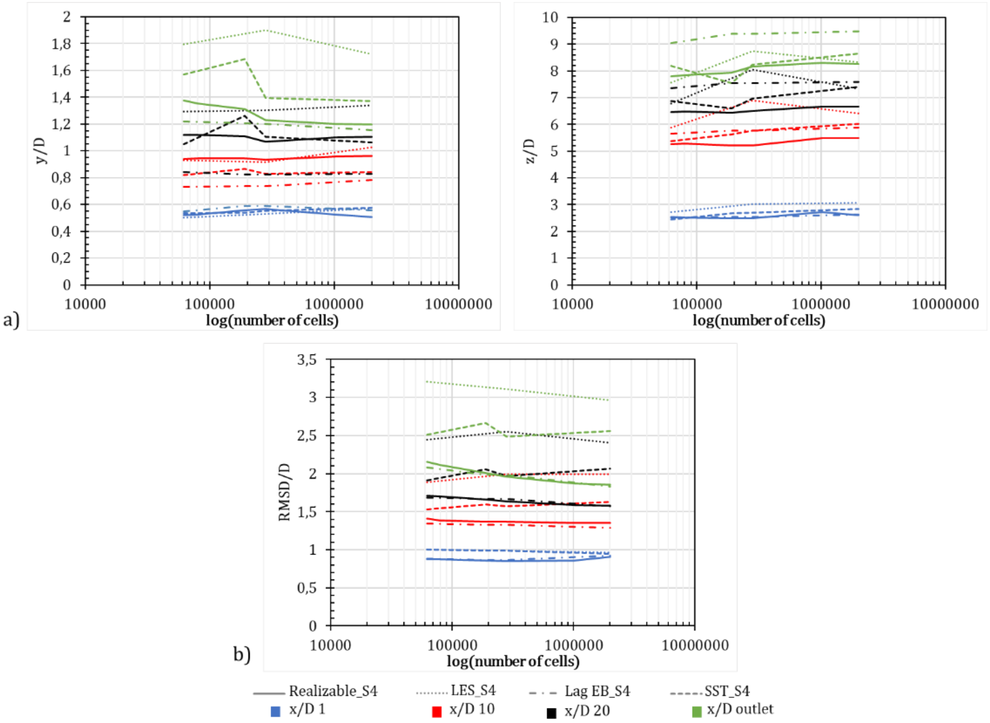

Figure 36. Results of strategy4 with various model including realizable k-epsilon, LES, lag EB and SST:
(a) Mass flow center of concentration on different x/D planes.
(b) Radial root mean square deviation of mass flow concentration on different x/D planes.

4.2 Additional investigation

4.2.1 Turbulent flow analysis

In contrast to time-averaged turbulence models such RANS, LES requires turbulent inflow boundary conditions to simulate turbulent flows [25]. Q-criterion formulated in terms of invariants of the velocity gradient tensor was used to visualize vorticity of turbulence for the whole LES simulation domain especially at the crossflow and nozzle inlets. A positive Q values represents that the turbulent flow field is dominated by rotation and vorticity. Q values were further visualized by generating iso surface, surface of constant value which is available in STAR-CCM+.

Figure 37 shows 3D isosurfaces of Q-criterion with threshold 15000 s^{-2}. The surface of the Q-value is colored by the velocity magnitude from the solution time of 6e-6 s which is time when the simulation was shifted from realizable k-epsilon model to unsteady LES model. The Q value of 15000 s^{-2} was chosen as the cut off value since the cut off provided good view of important turbulent vortices while excluding incoherent flows. It can be observed that no vortices were detected at the crossflow inlet except the near-wall region when LES was started after the initial solution from realizable k-epsilon at 6e-6 s. According to this, superimposed turbulent fluctuations should be applied in the future study of JIC in order to obtain a proper statistical distribution of eddies. This can be generated by synthetic eddy method [26] or by including flow contraction section with honey-comb structure as stated in Appendix A.

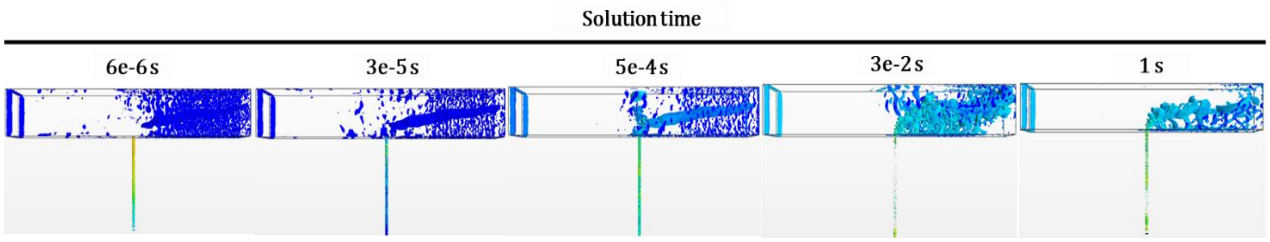

Figure 37. Q-criterion isosurface with threshold 15000 s^{-2} colored by velocity magnitude.

4.2.2 Dependency on turbulent Schmidt number

Turbulent Schmidt number (Sc_t) was used to describe turbulent mixing as mentioned in section 2.5. The standard approach in the earlier simulation of the study used 0.9 for Sc_t. In this investigation, the Sc_t was varied to evaluate its influence on mesh. The changes to Sc_t affected the whole concentration field as shown in Figure 38. However, the mixing in the jet core was well represented using higher Sc_t while the borders appeared to be better predicted using Sc_t lower than 0.9.

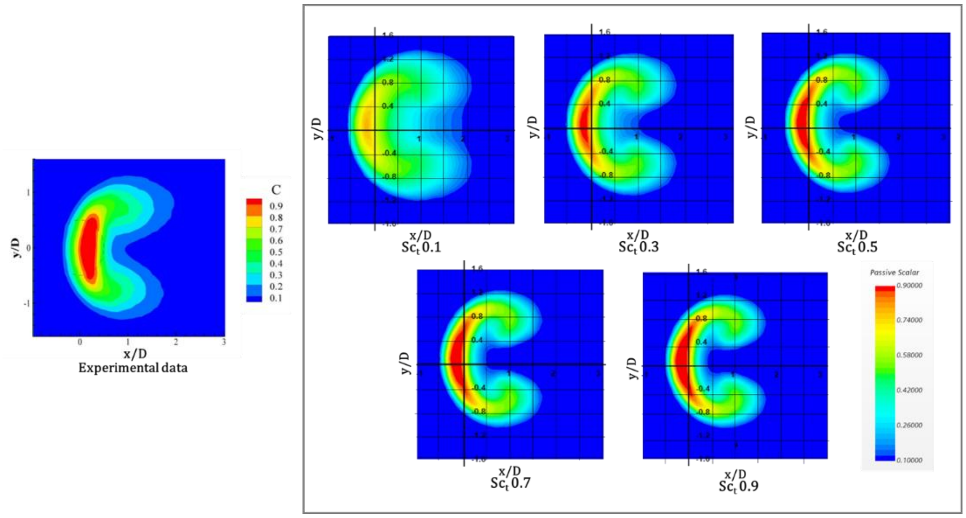

Figure 38. Influence of turbulent Sc: Two dimensional maps of dimensionless concentration at z/D=1.5.

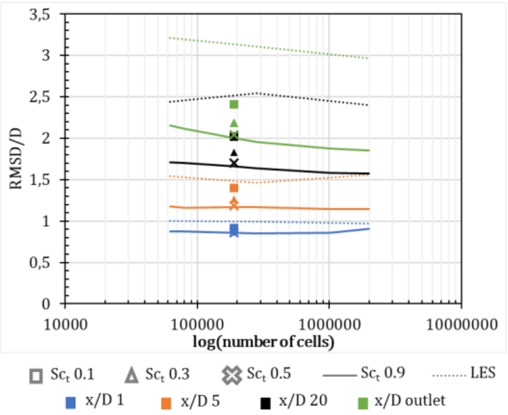

Figure 39. Influence of turbulent Sc on RMSD

Following the large effect of Sc_t on the concentration spread-out, RMSD was regarded as a suitable parameter to evaluate. Since RMSD obtained from LES simulation was higher than realizable k-epsilon model, Sc_t was gradually lowered in the realizable k-epsilon simulation in order to increase the spread-out of concentration to resemble the LES results. The results of Sc_t variation from 0.1 to 0.9 using realizable k-epsilon model are summarized in Figure 39. It is observed that lower Sc_t resulted in faster mixing due to higher turbulent diffusivity. Lowering Sc_t to 0.1 could only bring the simulation of realizable k-epsilon to LES approximately until x/D=5. For the region downstream, even though Sc_t was as low as 0.1, the RMSD of LES simulation was still higher. However, the common range of Sc_t for engineering applications is in the range between 0.5 to 0.9 [27]. Thus, lowering Sc_t down to 0.1 was too extreme which affected the jet core concentration field too much as seen in Figure 38. Hence $Sc_t \sim 0.5$ may be close to the optimum setting in order to reduce some of the deviation of the realizable k-epsilon model. However, it is clear that a Schmidt number correction is far from sufficient to compensate for other modeling drawbacks.

5. Conclusion

The simplification of air-fuel mixing in gas turbine burners using jet in crossflow configuration was applied to investigate the performance of 4 previously used mesh strategies which have recently been used in SGT-750, SGT-800 and other projects. The mesh strategies C1 and C2 did not provide good prediction of either velocity component or concentration when simulated either with realizable k-epsilon or LES turbulence models. This was due to unsuitable grid sizes concerning rules of thumbs for jet resolution. Also, the cell sizes included in mesh C1 and C2 were not in between the range of Kolmogorov and Taylor scale. On the other hand, mesh C3 and C4 revealed good agreement with experimental data for both velocity and concentration. According to this, mesh C3 and C4 were initially expected to be applied to the gas turbine models. However, since the C2 mesh strategy has been recently used in updated SGT-750 LES models which possesses three times larger amount of fuel nozzles as compared to the SGT-800 LES model where mesh C3 was retrieved, the computational cost would increase significantly if C3 strategy would be applied as standard. Therefore, further grid sensitivity test of C3 and C4 strategies were performed with the aim to possibly decrease number of cells to be the same as or at least close to the mesh C2 amount of 62k cells while achieving sufficient accuracy for both velocity component and concentration.

Adaptive mesh refinement based on concentration and velocity gradient was used to refine the mesh in the most important regions and to generate sufficiently fine meshes to investigate grid sensitivity. Mesh C4 occurred to be a more favorable mesh for further optimization since mesh C4 showed results more similar to the adaptive mesh. However, lowering the cell count of mesh C4 under 280k was not reliable enough due to grid dependence behavior of mesh C4.

A successful mesh optimization approach has been achieved in this study using mesh C4 together with adaptive mesh based on concentration gradient. Jet refinement region was the only part for alteration. The cones were introduced and placed attaching to the plane z=0 to achieve a better refinement near the wall. The geometrical shape parts of the cones were adjusted according to adaption cell sizes obtained from the gradient adapted mesh. The optimized mesh denoted as strategy4 exhibited high accuracy of velocity and concentration compared to available experimental data when using strategy4 with the realizable k-epsilon or LES turbulence models and showed the possibility to lower the cell count down to 62k cells for both turbulence models. Moreover, strategy4 fulfilled all cell sizes requirement for good flow resolution. More than 80% of the turbulent kinetic energy was resolved in the important jet region and small effect of unresolved scales was obtained when strategy4 was applied in LES simulation.

Turbulence model dependency test was also performed on strategy4. Four turbulence models including realizable k-epsilon, LES, lag EB k-epsilon and SST k-omega were selected. A large model dependency of strategy4 was found. Thus, the turbulence model was regarded as one of the important aspects to investigate in order to achieve reliable solution of the flow. Realizable k-epsilon and LES were observed to be best suitable for JIC simulation, while lag EB k-epsilon and SST k-omega models were not the best models to accurately predict JIC velocity component and concentration.

6. Future work

According to the turbulent flow analysis in section 4.2.1, no vortices were detected at the crossflow inlet except the near-wall region when LES was started. Since transient turbulent inflow boundary conditions are required for good LES simulation, synthetic turbulent fluctuations or contraction section with the honey-comb structure as stated in Appendix A should be applied in future studies of the JIC to analyze how it influences LES results.

Since measurement data were only available for the section shortly downstream of the nozzle, this numerical evaluation cannot be extended. Hence additional measurement data especially of the concentration field in the downstream region would strengthen this investigation. In this study, two additional parameters; mass flow center and radial root mean square deviation lack experimental data for validation. It would be highly beneficial if any future study collects these two parameters as well.

Lastly, the optimized mesh approach should be applied to the actual gas turbines models to optimize the distribution of fuel holes in the main channels of the combustor with the aim to achieve improved premixing of air and fuel in order to minimize NOx emission and/or improve capability of green fuels by improving flash back resistance etc.

References

[1] F. Galeazzo, G. Donnert, P. Habisreuther, N. Zarzalis, R. Valdes and W. Krebs, "Measurement and Simulation of Turbulent Mixing in a Jet in Crossflow," *Journal of Engineering for Gas Turbines and Power,* vol. 133, 2010.

[2] S. Chu and A. Majumdar, "Opportunities and challenges for a sustainable energy future," *Nature,* pp. 294-303, 2012.

[3] L. Caracciolo and P. A. Rubini, "Validation of a Partially-Premixed Combustion Model for Gas Turbine Applications," vol. 1, pp. 731-742, 2006.

[4] E. J. K. Nilsson, C. Brackmann, A. Abou-Taouk, J. Larfeldt and D. Moell, "Hydrogen Addition to Flames at Gas-Turbine-Relevant Conditions," Energiforsk Report, 2017.

[5] M. Safari, "Master Thesis Report: Geometrical improvement of SGT-750 burner," Linköpings universitet, Linköping, 2020.

[6] I. Sadrehaghighi, Mesh Generation in CFD, CFD Open Series, 2020.

[7] M. Boyce, Gas Turbine Engineering Handbook, Butterworth-Heinemann, 2011.

[8] L. Langston, "Turbines, Gas," in *Reference Module in Earth Systems and Environmental Sciences*, Elsevier, 2014.

[9] D. Koren, "Master Thesis Report: Computational Fluid Dynamics Unstructured Mesh Optimization for the Siemens 4th Generation DLE Burner," KTH, Royal Institute of Technology, 2015.

[10] "SGT-800," Siemens Energy AB, [Online]. Available: https://www.siemens-energy.com/global/en/offerings/power-generation/gas-turbines/sgt-800.html. [Accessed 10 May 2021].

[11] D. Lörstad, A. Lindholm, M. Björkman and I. Hultmark, "Siemens sgt-800 industrial gas turbine enhanced to 50mw: Combustor design modifications, validation and operation experience," *Proc. ASME Turbo Expo, GT2013-96478,* 2013.

[12] A. SOROUSH, "Master Thesis Report: CFD evaluation of a jet in cross flow related to gas turbine burner," Chalmers University of Technology, 2012.

[13] M. Persson, "Master Thesis Report: Combustion modelling using spray injectors in gas turbines," Linköpings universitet, 2018.

[14] A. Hellberg, "The Siemens SGT-750 gas turbine: developed for the oil and gas industry".

[15] Siemens, "Simcenter STAR-CCM+ Documentation," [Online]. Available: https://docs.sw.siemens.com/documentation/external/PL20201113103827399/en-

US/userManual/userguide/html/index.html#page/connect%2Fsplash.html. [Accessed 11 May 2021].

[16] B. Andersson, R. Andersson, L. Håkansson, M. Mortensen, R. Sudiyo and B. Van Wachem, Computational Fluid Dynamics for Engineers, Cambridge University Press, 2011.

[17] B. Launder and B. Sharma, "Application of the energy-dissipation model of turbulence to the calculation of flow near a spinning disc," *Letters in Heat and Mass Transfer,* vol. 1, no. 2, pp. 131-137, 1974.

[18] W. Jones and B. Launder, "The prediction of laminarization with a two-equation model of turbulence," *International Journal of Heat and Mass Transfer,* pp. 301-314, 1972 .

[19] S. Lardeau and F. Billard, "Development of an elliptic-blending lag model for industrial applications.," *54th AIAA Aerospace Sciences Meeting,* 2016.

[20] D. C. Wilcox, Turbulence Modeling for CFD, DCW Industries, 1998.

[21] C. Gurgiolo, M. Goldstein, W. Matthaeus, A. Viñas and A. Fazakerley, "Characteristics of the Taylor microscale in the solar wind/foreshock: magnetic field and electron velocity measurements," *Annales Geophysicae,* vol. 31, pp. 2063-2075, 2013.

[22] F. Ghasempour, R. Andersson and B. Andersson, "Multidimensional turbulence spectra – Statistical analysis of turbulent vortices," *Applied Mathematical Modelling,* p. 4226–4237, 2014 .

[23] P. E. Dimotakis, "Turbulent mixing," *Annual Review of Fluid Mechanics,* vol. 37, pp. 329-356, 2005.

[24] Y. Tominaga and T. Stathopoulos, "Turbulent Schmidt numbers for CFD analysis with various types of flowfield," *Atmospheric Environment,* vol. 41, no. 37, pp. 8091-8099, 2007.

[25] M. Klein, A. Sadiki and J. Janicka, "A digital filter based generation of inflow data for spatially developing direct numerical or large eddy simulations," *Journal of Computational Physics,* vol. 186, no. 2, p. 652–665, 2003.

[26] N. Jarrin, S. Benhamadouche, D. Laurence and R. Prosser, "A synthetic-eddy-method for generating inflow conditions for large-eddy simulations," *International Journal of Heat and Fluid Flow,* vol. 27, no. 4, pp. 585-593, 2006.

[27] C. Gualtieri, A. Angeloudis, F. Bombardelli, S. Jha and T. Stoesser, "On the Values for the Turbulent Schmidt Number in Environmental Flows," *Fluids,* vol. 2, 2017.

[28] C. E. Cárdenas, H. Bockhorn and R. Suntz, "Two-dimensional estimation of Reynolds-fluxes and -stresses in a Jet-in-Crossflow," *Applied Physics B: Lasers and Optics,* vol. 88, no. 4, pp. 581-591, 2007.

[29] "Reliable gas turbines," Siemens Energy AB, [Online]. Available: https://www.siemens-energy.com/global/en/offerings/power-generation/gas-turbines.html. [Accessed 9 May 2021].

[30] C. Soares, Gas turbines, A handbook of Air, Land and Sea Applications, 2014 .

[31] "Combustion section," [Online]. Available: http://www.aircav.com/gencombu.html. [Accessed 10 May 2021].

[32] S. D. I. Software, "Simcenter STAR-CCM+ Turbulence Modeling," [Online]. Available: https://web.cecs.pdx.edu/~gerry/class/ME448/lecture/pdf/STARCCM_Turbulence_Technical_Spotlight_Rich.pdf. [Accessed 12 May 2021].

Appendices

A. JIC experimental set up

The JIC set up retrieved from the reference [28] consisted of feed pipe crossflow, feed pipe jet and the flow channel of interest as depicted in Figure 40. A fan was installed to feed the air in the crossflow system. Venturi tubes and rotameter were also included to control the flow rate of the feed air. Aerosol droplets were added as particles tracer using a particle generator for Particle Image Velocimetry (PIV) measurement as shown in the figure. Afterwards, the air entered the diffusor section for the purpose to expand the flow from circular to quadratic cross section. Air then entered the smoothing section where fluctuation of air flow was reduced by the mean of honey-comb structure. Later, nozzle section had a role to contract the cross-sectional area of the air flow to JIC measuring section of 108*108 mm.

For the jet part, compressed air with mass flow controllers were included in the system together with NO_2 as a tracer for Laser Induced Fluorescence (LIF) measurement. The jet pipe with diameter of 8 mm and length of 250 mm was mounted to crossflow wall. This jet nozzle was located 328 mm downstream from the inlet of the crossflow channel. The geometrical data of the measuring section can be clearly seen in Figure 9.

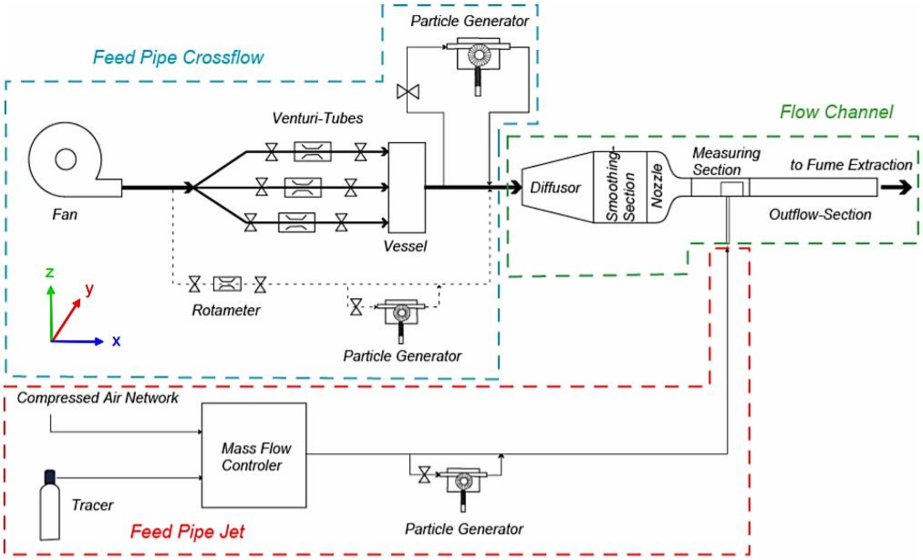

Figure 40. JIC experimental arrangement [28].

B. Previously used mesh strategies

B1. Mesh strategies in details

This section includes details of geometrical shape parts and cell sizes in each previously used mesh strategies which were obtained from the SGT-750 and SGT-800 models. Note that the cell sizes represented here denotes the computational grid after applying JIC scaling factor.

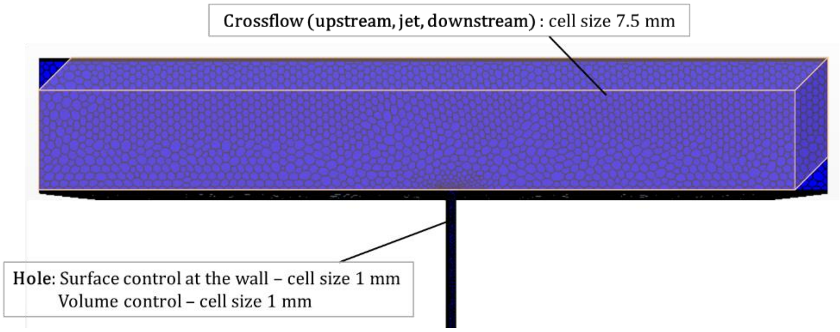

Figure 41. Mesh C1 details.

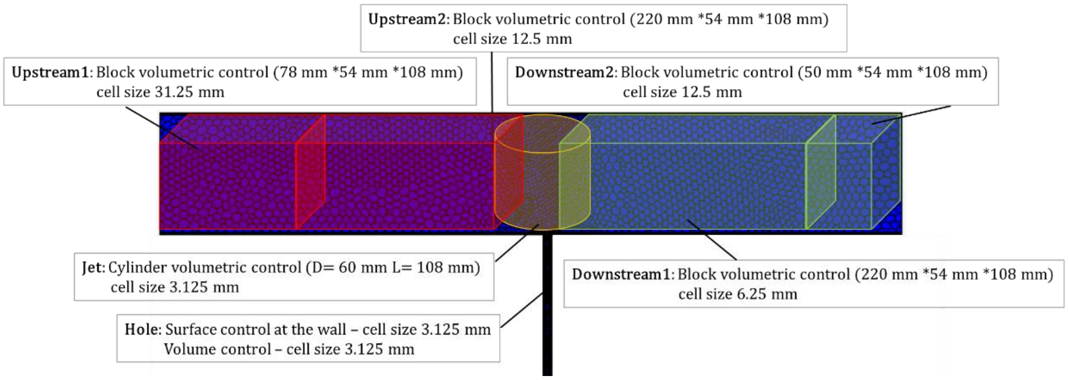

Figure 42. Mesh C2 details.

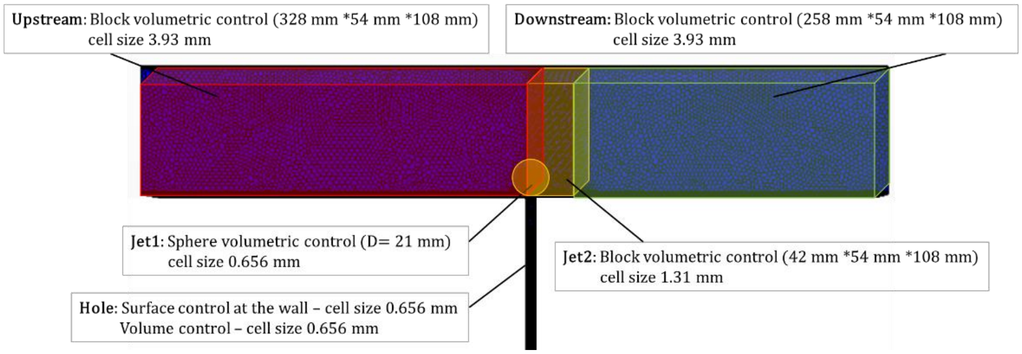

Figure 43. Mesh C3 details.

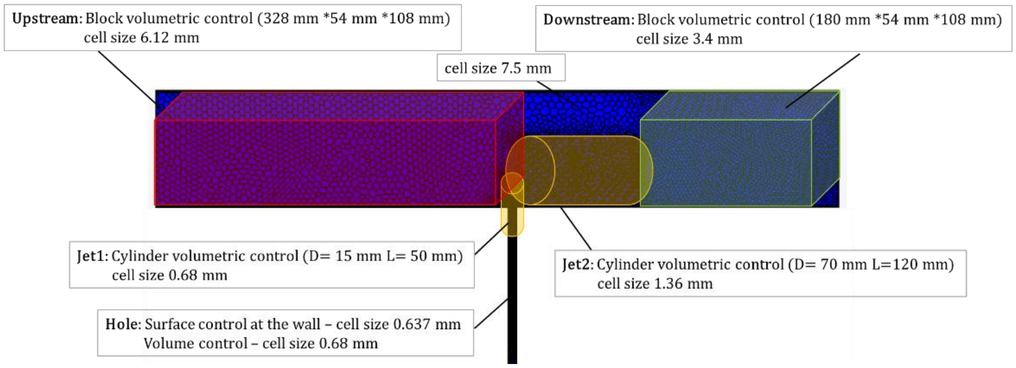

Figure 44. Mesh C4 details.

B2. Grid sensitivity test of mesh C3 and C4

For overall grid sensitivity test on mesh C3 and C4 when the mesh with highest cell count from 4th level refinement of adaptive mesh were included as shown in Figure 45 and Figure 46, mesh C3 and C4 showed similar results of velocity component and concentration. Accurate prediction of both parameters was obtained for both mesh C3 and C4 when the meshes were coarsened to 62k cells.

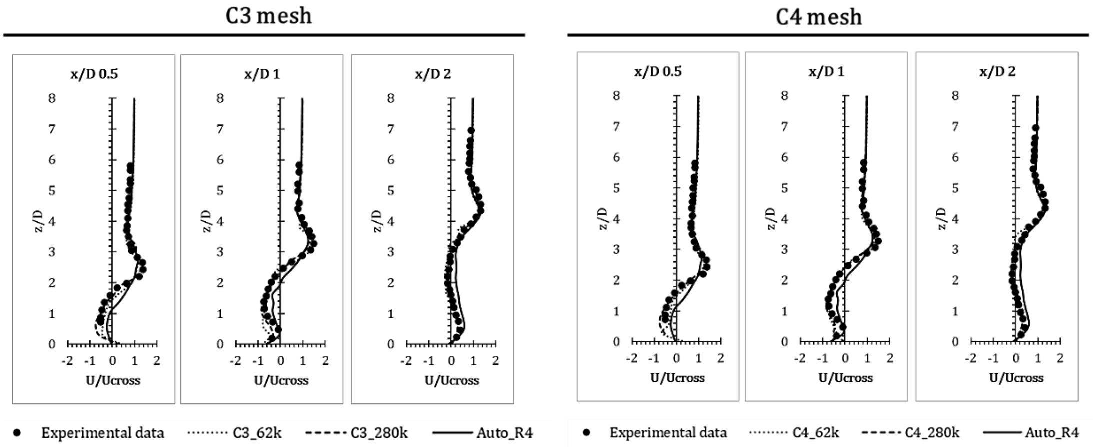

Figure 45. Results of mesh C3 and C4: Velocity component at symmetry plane y=0.

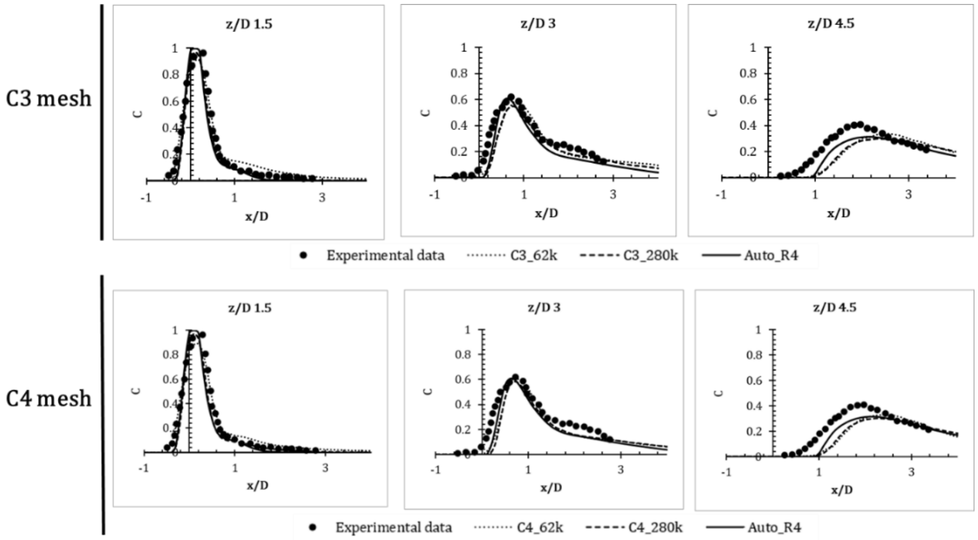

Figure 46. Results of mesh C3 and C4: Dimensionless concentration at symmetry plane y=0.

C. Turbulence model dependence of the optimized mesh

This section presents velocity and concentration profiles of the optimized mesh for different turbulence models: realizable k-epsilon, LES, lag EB k-epsilon and SST k-omega models.

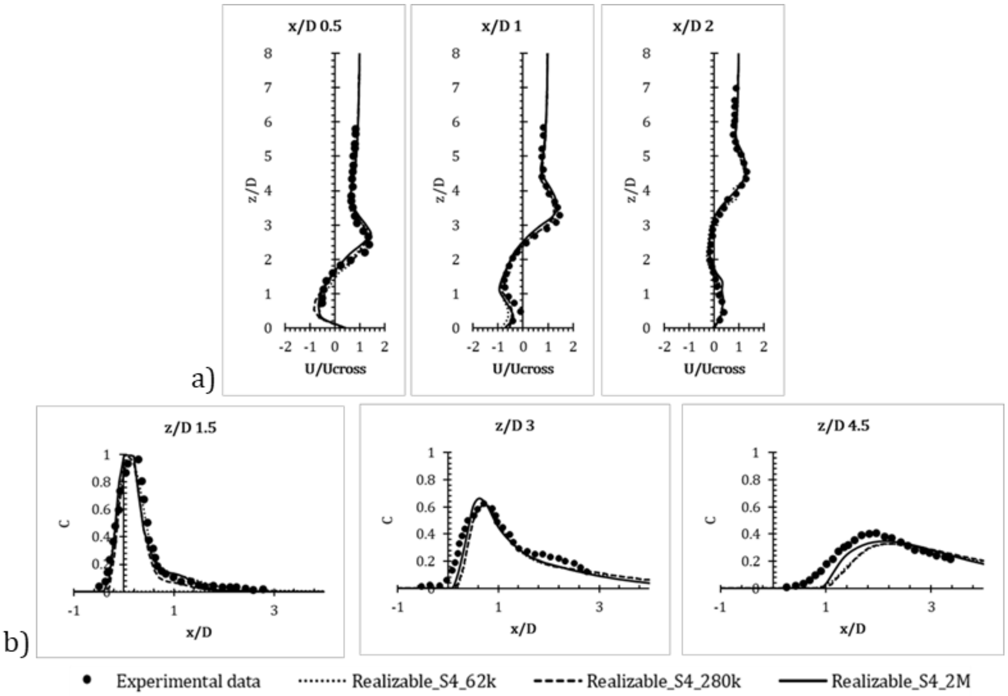

Figure 47. Results of strategy4 with realizable k-epsilon: (a) Velocity component at symmetry plane y=0. (b)Dimensionless concentration at symmetry plane y=0.

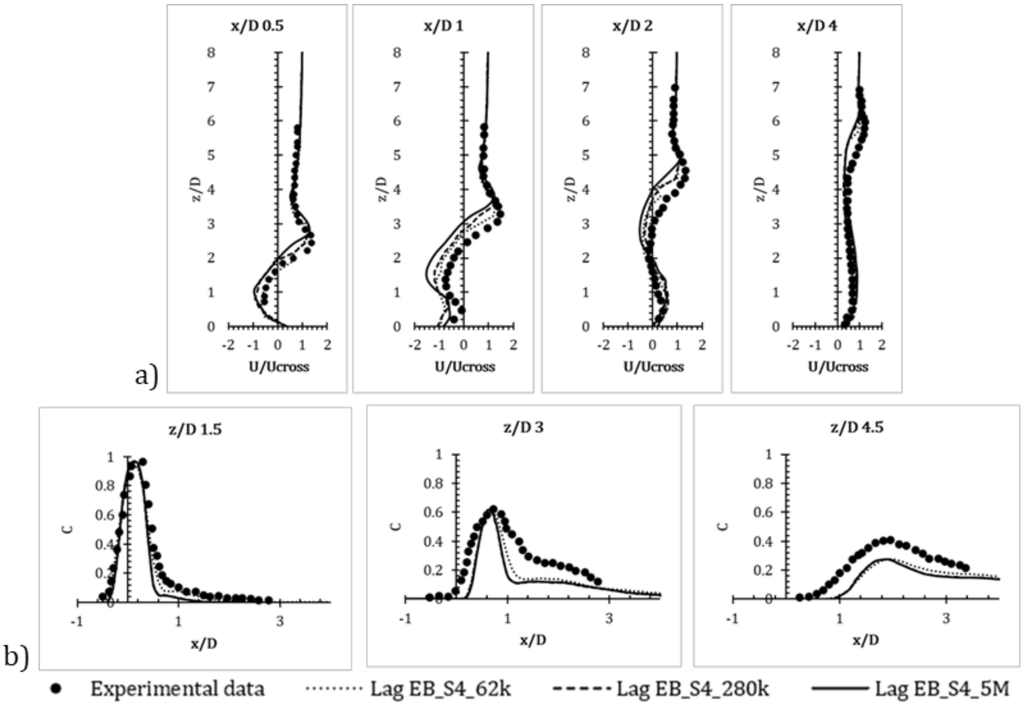

Figure 48. Results of strategy4 with lag EB model: (a) Velocity component at symmetry plane y=0. (b)Dimensionless concentration at symmetry plane y=0.

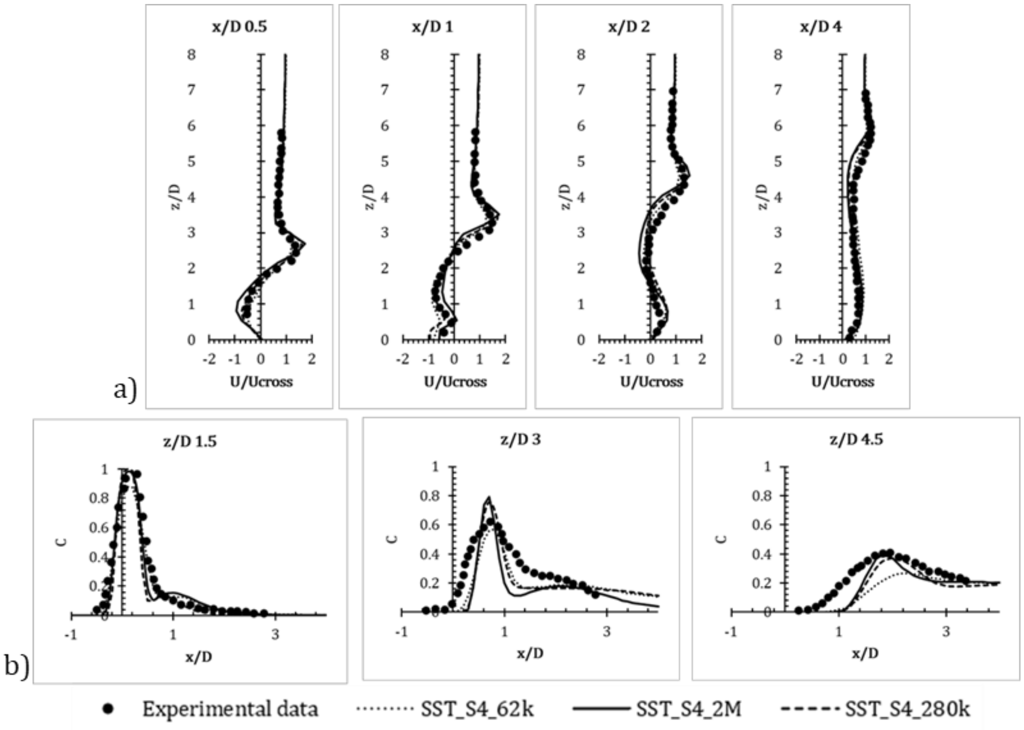

Figure 49. Results of strategy4 with SST model: (a) Velocity component at symmetry plane y=0. (b)Dimensionless concentration at symmetry plane y=0.

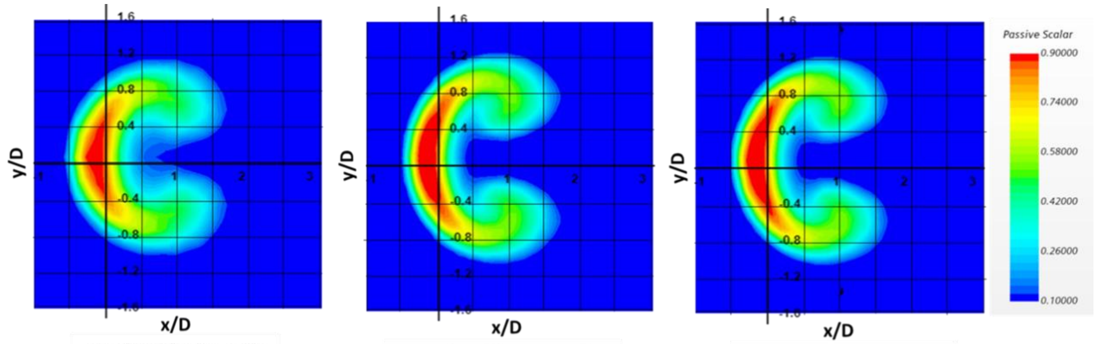

Realizable_S4_62k Realizable_S4_280k Realizable_S4_2M

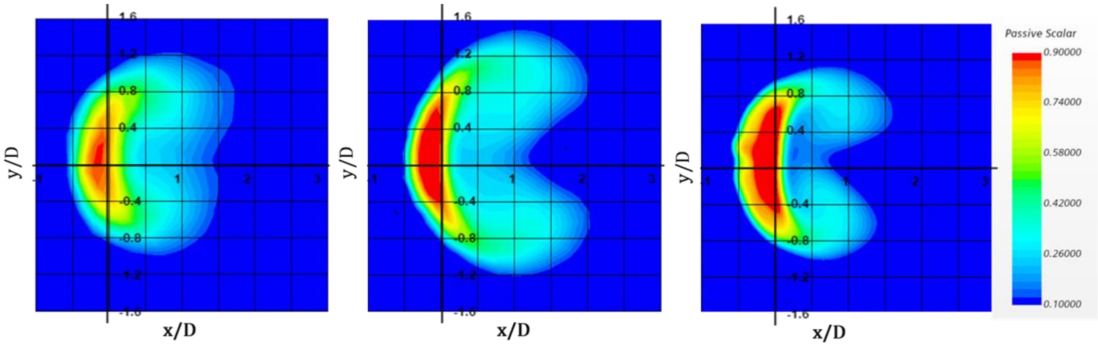

LES_S4_62k LES_S4_280k LES_S4_2M

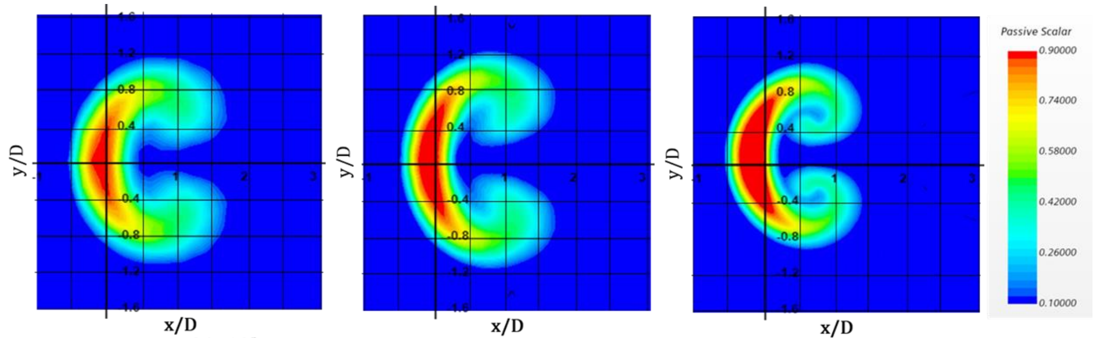

Lag EB_S4_62k Lag EB_S4_280k Lag EB_S4_2M

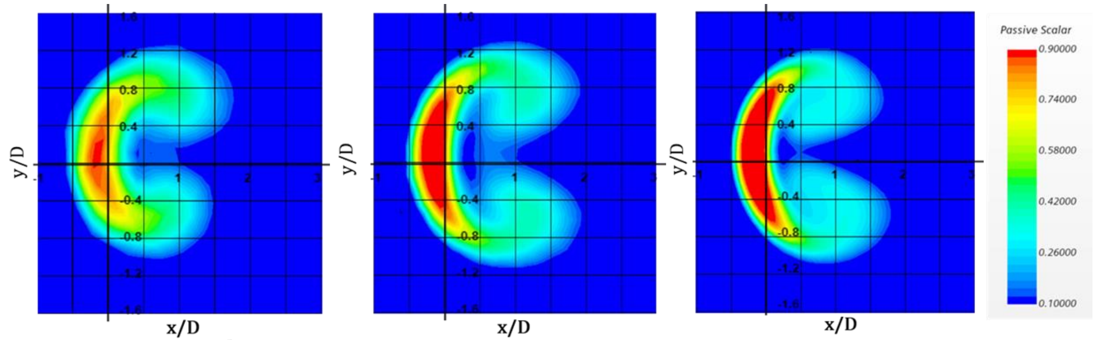

SST_S4_62k SST_S4_280k SST_S4_2M

Figure 50. Results of strategy4 with various models: Two dimensional maps of dimensionless concentration at z/D=1.5.

DEPARTMENT OF CHEMISTRY AND CHEMICAL ENGINEERING
CHALMERS UNIVERSITY OF TECHNOLOGY
Gothenburg, Sweden
www.chalmers.se

CHALMERS
UNIVERSITY OF TECHNOLOGY